

# Generative Ensemble-Regression: Learning Stochastic Dynamics from Discrete Particle Ensemble Observations

Liu Yang<sup>1</sup>, Constantinos Daskalakis<sup>2</sup>, and George Em Karniadakis<sup>1,3</sup>

<sup>1</sup>Division of Applied Mathematics, Brown University, Providence, RI 02912, USA

<sup>2</sup>Department of Electrical Engineering and Computer Science, Massachusetts Institute of Technology, Cambridge, Massachusetts, USA

<sup>3</sup>Pacific Northwest National Laboratory, Richland, WA 99354, USA

## Abstract

We propose a new method for inferring the governing stochastic ordinary differential equations by observing particle ensembles at discrete and sparse time instants, i.e., multiple “snapshots”. Particle coordinates at a single time instant, possibly noisy or truncated, are recorded in each snapshot but are unpaired across the snapshots. By training a generative model that generates “fake” sample paths, we aim to fit the observed particle ensemble distributions with a curve in the probability measure space, which is induced from the inferred particle dynamics. We employ different metrics to quantify the differences between distributions, like the sliced Wasserstein distances and the adversarial losses in generative adversarial networks. We refer to this approach as generative “ensemble-regression”, in analogy to the classic “point-regression”, where we infer the dynamics by performing regression in the Euclidean space, e.g. linear/logistic regression. We illustrate the ensemble-regression by learning the drift and diffusion terms of particle ensembles governed by stochastic ordinary differential equations with Brownian motions and Lévy processes up to 20 dimensions. We also discuss how to treat cases with noisy or truncated observations, as well as the scenario of paired observations, and we prove a theorem for the convergence in Wasserstein distance for continuous sample spaces.

**Keywords:** data-driven dynamic inference, physics informed learning, stochastic ODEs, Fokker-Planck equations, GANs, sliced Wasserstein distance, Lévy process

# 1 Introduction

Classic methods for inferring the dynamics from data usually require observations of a point at discrete time instants; we name this classic paradigm as “point-regression”. More specifically, as is illustrated in Figure 1, in point-regression problems we want to infer the initial coordinate as well as the governing ordinary differential equation (ODE) of a point, given the (possibly noisy) observations of its coordinates at discrete time instants. Typically, we optimize the dynamics and the initial coordinate so that the coordinates on the inferred curve match the coordinates from data. More formally, the weighted summation of Euclidean distances, sometimes applied with certain functions, is minimized. In some cases we may have observations of multiple points, but the coordinates are supposed to be labeled with point indices so that we can deal with individual points separately.

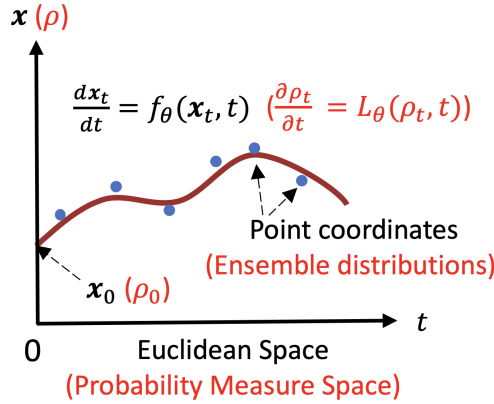


Figure 1: Schematic showing the two paradigms of point-regression and ensemble-regression for dynamic inference. In point-regression problems (black legends), we aim to fit the point coordinates (blue dots) from data with the inferred curve (brown curve), determined by the initial coordinate  $\mathbf{x}_0$  as well as the dynamics  $d\mathbf{x}_t/dt = f_\theta(\mathbf{x}_t, t)$ , where  $f_\theta$  is a deterministic function in the Euclidean space. As an analogue, in ensemble-regression problems (red legends), we aim to fit the distributions of the ensemble in the snapshots (blue dots) with the inferred curve (brown curve), determined by the initial distribution  $\rho_0$  as well as the dynamics  $\partial\rho_t/\partial t = L_\theta(\rho_t, t)$ , where  $L_\theta$  is an operator in the probability measure space.

Let us consider, for simplicity, the one-dimensional linear regression with quadratic loss as an example. Given observations of  $x$  at multiple  $t$ , we want to optimize the parameter  $a$  in the ODE  $dx_t/dt = a$  as well as the initial point  $x_0 = b$  so that the mean squared  $L_2$  distance between predictions and data points is minimized, where  $a$  and  $b$  are the slope and the intercept of the linear function. Other examples in this category include logistic regression, recurrent

neural networks and the neural ODE for time series [1], sparse identification of nonlinear dynamics (SINDy) [2], etc.

In this paper we propose a new approach for dynamic inference. Specifically, we wish to use observations of a particle ensemble at discrete time instants to learn the governing dynamics of the particles, especially stochastic ones. We call an observation at a single time instant a “snapshot”, where part or all of the particle coordinates in the ensemble are recorded. We emphasize that we do not need the coordinates labeled with particle indices in the observations, i.e., we do not require the particles to be paired across snapshots. In fact, all the information we need from the snapshots is the particle distributions at different time instants.

We name this paradigm “ensemble-regression” in analogy to the “point-regression”. In particular, as is illustrated in Figure 1, given ensemble snapshots at different moments, we want to infer the initial distribution as well as the governing stochastic ordinary differential equation (SODE) of the particles. The SODE for particles would also induce a curve  $t \rightarrow \rho_t$  in the probability measure space for the particle distributions, governed by a corresponding deterministic PDE shown in Figure 1<sup>1</sup>. We aim to optimize the dynamics and the initial distribution so that the distributions on the inferred curve in the probability measure space match the distributions from the data. More formally, we aim to minimize the weighted summation of “metrics of differences between distributions”, sometimes applied with certain functions. *In short, we can view this approach as performing regression in the probability measure space equipped with certain metrics of differences.* In this paper we use the sliced Wasserstein (SW) distance [3] and the adversarial loss for the generator in generative adversarial networks (GANs) [4, 5, 6] as two examples of such metrics. Note that the ensemble-regression proposed here is different from the classic “ensemble methods” [7], where an ensemble of learners with multiple learning algorithms are combined for better performance.

We summarize the analogy between point-regression and ensemble-regression in Table 1.

Table 1: Analogy between point-regression and ensemble-regression.

	point-regression	ensemble-regression
space	Euclidean space	probability measure space
dynamics	ODE	SODE(particles), PDE(measures)
goal	fit individual points	fit particle ensembles
metrics	Euclidean distance, etc.	SW distance, GAN loss, etc.

In this paper, we focus on the problems where the particles are driven by a deterministic drift field with a Brownian noise or Lévy noise. Such dynamics for the particles will induce a Fokker-Planck equation as the governing equation for the particle distributions, where the Laplacian operator needs to be replaced

<sup>1</sup>Here  $\rho_t$  is a measure and the PDE is in the sense of distribution.

by the fractional Laplacian for the Lévy case. To represent the inferred curve in the probability measure space, we build a *generative model* consisting of a feed-forward neural network, which maps from Gaussian noise to the initial distribution, as well as a discretized SODE with trainable variables, where we encode our partial knowledge of the particle dynamics, to generate “fake” sample paths, whose marginal distribution at time  $t \geq 0$  will be used to represent  $\rho_t$  on the curve of probability measures. The discretized SODE with unknown terms parameterized as neural networks is also known as the “neural SDE” in the literature [8, 9, 10, 11, 12]. We will also introduce several augmentations to the generative model to deal with the heavy tails in the target distribution, noisy observations, and truncated observations.

In [13] the authors used a similar idea to infer the stochastic dynamics, i.e. training a generative model to match distributions. However, their problem setup and detailed methodology is totally different from ours, in that they use noisy observations of a sample path as the data, where the coordinates are of course paired, and instead of matching the distributions of particle ensembles, they aim to match the distributions of the hidden derivatives. Moreover, based on the Gaussian process, their approach cannot be easily applied to SODE problems with non-Gaussian noise. Actually, most stochastic dynamic inference algorithms are based on calculating or approximating the probability of observations of a sample path conditioned on the system parameters, using Euler-Maruyama discretization [14, 15], Kalman filtering [16], variational Gaussian process-based approximation [17, 18], the Fokker-Planck-Kolmogorov equations [19, 20], etc. Other related work includes [21], where GANs were applied to learn the distribution of the parameters and solutions in time-independent stochastic differential equations, and [22] where GANs were applied to learn the distribution of the random parameters estimated from the (paired) observations of individual ODEs.

We should remark that even if we know the macroscopic distribution at any time  $t$ , i.e., the curve  $t \rightarrow \rho_t$  in Figure 1 is given, the dynamics of individual particles in the microscopic scale, i.e., the governing SODE is, in general, not unique. For example, the following two dynamics of individual particles with  $\mathcal{N}(0, 1)$  as the initial distribution will lead to the same curve  $\rho_t = \mathcal{N}(0, t + 1)$  in the probability measure space:

1. Standard Brownian motion with no drift.
2.  $dx_t/dt = x_t/(2t + 2)$  with no diffusion, i.e.,  $x_t = x_0\sqrt{t + 1}$ .

However, it is possible to obtain uniqueness of microscopic dynamics if we limit the candidates in a small family. For example, for the continuity equation  $d\rho_t/dt = -\nabla \cdot (\mathbf{v}_t \rho_t)$ , for any curve  $t \rightarrow \rho_t$  absolutely continuous from  $[a, b]$  to  $\mathcal{P}_2(\mathbb{R}^d)$ , where  $\mathcal{P}_2(\mathbb{R}^d)$  is the Wasserstein-2 space of probability measures with finite quadratic moments in  $\mathbb{R}^d$ , there exists a unique curve  $t \rightarrow \mathbf{v}_t$ , where  $\mathbf{v}_t$  is limited to the  $L^2(\mu_t; \mathbb{R}^d)$  closure of  $\{\nabla\varphi : \varphi \in C_c^\infty(\mathbb{R}^d)\}$  [23, 24]. In real-world problems, the choice of the family actually requires our partial knowledge of the

dynamic system, which can be encoded into the generative model as mentioned above.

The rest of the paper is organized as follows: In Section 2, we formulate the problems we aim to solve. In Section 3, we present the details of our method, including the generative model, loss function, and augmentations to the generative model for various cases. We show the computational results in Section 4. In addition, in Section 5 we present a discussion on the scenario of paired observations. We present a summary in Section 6. Furthermore, in Appendix A we introduce the  $\alpha$ -stable random variable generator used for the SODE problems with Lévy process; in Appendix B we introduce the sliced Wasserstein distance; in Appendix C we show the effect of increasing the training data on the precision of inference; in Appendix D we prove the theorem for the convergence in Wasserstein distance for continuous sample spaces; finally, in Appendix E we provide a counter-example.

## 2 Problem Setup

We consider a system with an ensemble of particles governed by the following stochastic differential equation:

$$d\mathbf{X}_t = \boldsymbol{\mu}_t dt + d\mathbf{Z}_t, \quad t \geq 0, \quad (1)$$

where  $\mathbf{X}_t \in \mathbb{R}^d$  is the position of a particle at time  $t$ ,  $\boldsymbol{\mu}_t \in \mathbb{R}^d$  is the deterministic drift force, and  $d\mathbf{Z}_t$  is the stochastic term. We use  $\rho_t$  to denote the distribution of  $\mathbf{X}_t$ .

The most commonly used stochastic processes in physics and biology are diffusion processes and Levy processes. For  $\mathbf{X}_t$  as a diffusion process, we could write Equation 1 as

$$d\mathbf{X}_t = \boldsymbol{\mu}_t dt + \boldsymbol{\sigma}_t d\mathbf{B}_t, \quad t \geq 0, \quad (2)$$

where  $\mathbf{B}_t$  is the  $d$ -dimensional standard Brownian motion and  $\boldsymbol{\sigma}_t \in \mathbb{R}^{d \times d}$  is the diffusion coefficient. The probability density function  $p(\mathbf{x}, t)$  for  $\mathbf{X}_t$  will then be governed by the Fokker-Planck equation:

$$\frac{\partial}{\partial t} p = -\nabla \cdot (\boldsymbol{\mu}_t p) + \frac{1}{2} \nabla \cdot (\nabla \cdot (\boldsymbol{\sigma}_t \boldsymbol{\sigma}_t^T p)). \quad (3)$$

For  $\mathbf{X}_t$  as a Levy process, we have a different term on the right-hand-side of Equation 2, i.e.,

$$d\mathbf{X}_t = \boldsymbol{\mu}_t dt + \boldsymbol{\epsilon}_t d\mathbf{L}_t^\alpha, \quad t \geq 0, \quad (4)$$

where  $\mathbf{L}_t^\alpha$  is the  $\alpha$ -stable symmetric Lévy process.

We consider the scenario where the data available are the observations of the particles at different time instants  $\{t_i\}_{i=1}^n$  with  $0 \leq t_1 < t_2 \dots < t_n$ . More formally, the available data are  $\{\mathcal{D}_i\}_{i=1}^n$ , where  $\mathcal{D}_i = \{\mathbf{X}_{t_i}(\omega_{i,j})\}_{j=1}^{N_i}$  is a set of  $N_i$  observations of  $\mathbf{X}_{t_i}$  with hidden random states  $\{\omega_{i,j}\}_{j=1}^{N_i}$ . In other words,  $\mathcal{D}_i$  is a set of samples drawn from  $\rho_{t_i}$ .

In the cases where  $\omega_{1,j} = \omega_{2,j} \dots = \omega_{n,j}$  for all  $j$ , we know that  $\{\mathbf{X}_{t_i}(\omega_{i,j})\}_{i=1}^n$  comes from the same sample path for a fixed  $j$ , and we refer to these cases as the “paired” observations. In other cases where  $\{\mathbf{X}_{t_i}(\omega_{i,j})\}_{i=1}^n$  does not come from the same sample path for a fixed  $j$ , we refer to these cases as the “unpaired” observations. Sometimes the observations come from the same batch of sample paths, but we cannot distinguish the particles in the ensemble, thus cannot assign the observations with the particle indices. This also belongs to the “unpaired” case. In this paper we mainly focus on the unpaired case, and present some discussions on the paired case in Section 5. In addition, we may have noisy observations and truncated data, i.e., with observations available only in some regions.

In forward problems, we assume that we have full knowledge of  $\boldsymbol{\mu}_t$ ,  $\boldsymbol{\sigma}_t$  and  $\boldsymbol{\epsilon}_t$ , and we aim to infer  $\rho_t$  for  $t \geq 0$ . We emphasize that in this paper we do not have full knowledge of  $\rho_0$  as in the traditional forward problem setup. Instead, the available data are the limited samples of  $\mathbf{X}_t$  at  $t = t_1, t_2, \dots, t_n$ . Note that the limited samples at a fixed time  $t$  will inevitably lead to errors when estimating  $\rho_t$ , but we wish to make use of the SODE and the observations in multiple snapshots to reduce the error.

In inverse problems, we may be unaware of some of  $\boldsymbol{\mu}_t$ ,  $\boldsymbol{\sigma}_t$  and  $\boldsymbol{\epsilon}_t$ , or we may only know the parametrized forms of these terms, and we aim to infer these terms directly (or the parameters) as well as  $\rho_t$  for  $t \geq 0$ . While  $\boldsymbol{\mu}_t$ ,  $\boldsymbol{\sigma}_t$  and  $\boldsymbol{\epsilon}_t$  could be functions of  $\mathbf{X}_t$  and  $t$  in general, as a demonstration, in this paper we focus on the cases where they are constants or functions of  $\mathbf{X}_t$  but independent of  $t$ .

### 3 Methodology

In this section, we will first introduce the main framework of generative ensemble-regression, including the generative model and the loss functions. We will then introduce some techniques for the cases characterized by distributions with heavy tails, or the observations are noisy or truncated.

#### 3.1 A Generative Model for SODEs

As mentioned in the introduction, we use a generative model to represent the inferred curve in the probability measure space. As illustrated in Figure 2, we use the generative model to generate “fake” sample paths, whose marginal distribution at time  $t \geq 0$  will be used to represent  $\rho_t$  on the curve of probability measures.

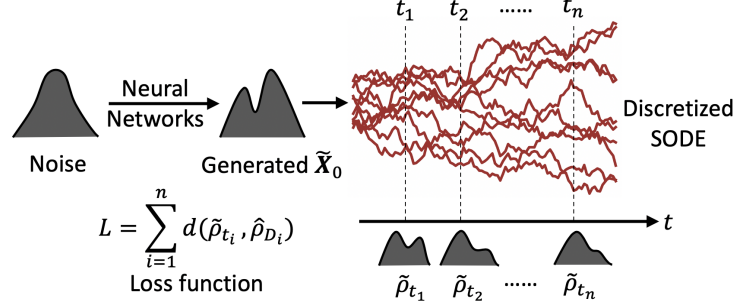


Figure 2: Schematic of the generative model for ensemble-regression. We first use a feed-forward neural network to map the input Gaussian noise to the output  $\tilde{\mathbf{X}}_0 \in \mathbb{R}^d$ , whose distribution  $\tilde{\rho}_0$  is intended to approximate the initial distribution  $\rho_0$ . Subsequently, we apply the discretized SODE with trainable parameters to generate sample paths  $\tilde{\mathbf{X}}_t$  for  $t > 0$  with  $\tilde{\mathbf{X}}_0$  as the initial condition (brown curves). We then measure the differences between the distributions of generated samples  $\tilde{\mathbf{X}}_t$  and the snapshots from data as our loss function.

We firstly use a feed-forward neural network  $G_\theta$  parameterized by  $\theta$  as a generator, which takes samples from a  $d$ -dimensional Gaussian distribution  $\mathcal{N}$  as input and outputs samples from the generated distribution  $\nu_\theta = G_{\theta\#}\mathcal{N}$ , where  $G_{\theta\#}\mathcal{N}$  denotes the push forward of  $\mathcal{N}$  by  $G_\theta$ . We intend to use  $\nu_\theta$  to approximate  $\rho_0$ , i.e., the distribution of  $\mathbf{X}_0$ .

In forward problems, using a discretized version of Equation 1 we can draw samples of  $\mathbf{X}_t$  for any  $t > 0$  with  $G_{\theta\#}\mathcal{N}$  as the initial distribution. For example, if  $\mathbf{X}_t$  is a diffusion process in Equation 2, we can use the following forward Euler scheme:

$$\begin{aligned} \tilde{\mathbf{X}}_0 &= G_\theta(\mathbf{z}), \quad \mathbf{z} \sim \mathcal{N} \\ \tilde{\mathbf{X}}_{(i+1)\Delta t} &= \tilde{\mathbf{X}}_{i\Delta t} + \boldsymbol{\mu}_t \Delta t + \boldsymbol{\sigma}_t \sqrt{\Delta t} \boldsymbol{\xi}_i, \quad i \geq 0, \end{aligned} \quad (5)$$

where  $\Delta t$  is the time step, and  $\boldsymbol{\xi}_i$  are i.i.d. standard Gaussian random variables. If  $\mathbf{X}_t$  is a Levy process in Equation 4, the forward Euler scheme is:

$$\begin{aligned} \tilde{\mathbf{X}}_0 &= G_\theta(\mathbf{z}), \quad \mathbf{z} \sim \mathcal{N} \\ \tilde{\mathbf{X}}_{(i+1)\Delta t} &= \tilde{\mathbf{X}}_{i\Delta t} + \boldsymbol{\mu}_t \Delta t + \epsilon_t \Delta t^{1/\alpha} \boldsymbol{\zeta}_{\alpha,i}, \quad i \geq 0, \end{aligned} \quad (6)$$

where  $\boldsymbol{\zeta}_{\alpha,i}$  are i.i.d.  $\alpha$ -stable random variables. The method to generate  $\alpha$ -stable random variables in TensorFlow is presented in Appendix A. In the following, we use  $\tilde{\rho}_t$  to denote the distribution of  $\tilde{\mathbf{X}}_t$ .

In inverse problems, we replace the unknown terms in Equations 5 and 6 with neural networks, or replace the unknown parameters with trainable variables if we know the parametrized form of these terms. We use  $\phi$  to denote the trainable variables and the parameters in the neural networks for the unknown terms. We remark that the loss functions for forward and inverse problems are identical,

which we will introduce in the next subsection, but the variables to train are  $\theta$  in forward problems, while  $\theta$  and  $\phi$  in inverse problems.

One may use  $\hat{\rho}_{\mathcal{D}_1}$  as an approximation of  $\rho_{t_1}$ , and draw samples of  $\mathbf{X}_t$  for  $t \geq t_1$  with discretized SODEs as in Equation 5 and 6. While this strategy could remove the generator  $G_\theta$  and might outperform the method introduced above in some cases, we also point out that it has the following limitations:

1. We cannot infer  $\rho_t$  for  $0 \leq t < t_1$  if  $0 < t_1$ .
2. As we mentioned in the previous section, we wish to make use of the SODE and the observations at multiple moments to reduce the error from limited samples. The error arising from the difference between  $\hat{\rho}_{\mathcal{D}_1}$  and  $\rho_{t_1}$  could never be removed with such a strategy.
3. This strategy can hardly handle the scenario, where we have noisy observations or truncated data in  $\mathcal{D}_1$ .

Due to the above limitations, we do not dive into this strategy in the present paper.

### 3.2 Loss functions

If the inferred initial distribution and unknown terms match the real ones perfectly, then  $\tilde{\rho}_t$  should be equal to  $\rho_t$  if we neglect the errors coming from the numerical integration. Motivated by this observation, we tune the parameters in our generative model using training data  $\{\mathcal{D}_i\}_{i=1}^n$ , so that  $\tilde{\rho}_{t_i}$  fits  $\mathcal{D}_i$  for each  $i$ . Upon convergence of training, ideally  $\tilde{\rho}_t$  should approximate  $\rho_t$ , and thus we can estimate the density or statistics of  $\rho_t$  using  $\tilde{\mathbf{X}}_t$ .

In order to train the generative model, we need to define a distance function  $d(\cdot, \cdot)$  to measure the difference between the two input distributions, which can be estimated from samples drawn from the two distributions. Consequently, the loss function is defined as:

$$L = \sum_{i=1}^n d(\tilde{\rho}_{t_i}, \hat{\rho}_{\mathcal{D}_i}), \quad (7)$$

where  $\hat{\rho}_{\mathcal{D}_i}$  is the empirical distribution induced from the sample set  $\mathcal{D}_i$ .

In this paper we employ two approaches to quantify the distance:

1. We choose the squared sliced Wasserstein-2 (SW) distance [3] as the function  $d$ . We present the details of the definition as well as the estimation of SW distance in Appendix B. Note that the sliced Wasserstein-2 distance is exactly the Wasserstein-2 distance in the 1D case. Moreover, the slice Wasserstein-2 distance and Wasserstein-2 distance induce the same topology on compact sets [25], i.e., the convergence in slice Wasserstein-2 distance is equivalent to the convergence in Wasserstein-2 distance.



2. We use GANs to provide the metric: for each  $i$ , we use a discriminator  $D_i$  to be the critic for generated samples  $\tilde{\mathbf{X}}_{t_i}$  and real samples from  $\mathcal{D}_i$ . Then, the adversarial loss given by  $D_i$  can act as a metric of the difference between  $\tilde{\rho}_{t_i}$  and  $\hat{\rho}_{\mathcal{D}_i}$ . In particular, we use WGAN-GP as our version of GANs in our paper, with the loss function for each discriminator  $D_i$  defined as

$$L_{D_i} = \mathbb{E}_{\tilde{\mathbf{X}}_{t_i} \sim \tilde{\rho}_{t_i}} [D_i(\tilde{\mathbf{X}}_{t_i})] - \mathbb{E}_{\mathbf{X}_{t_i} \sim \hat{\rho}_{\mathcal{D}_i}} [D_i(\mathbf{X}_{t_i})] + \lambda \mathbb{E}_{\hat{\mathbf{x}}_i \sim \rho_{\hat{\mathbf{x}}_i}} [(\|\nabla_{\hat{\mathbf{x}}_i} D_i(\hat{\mathbf{x}}_i)\|_2 - 1)^2], \text{ for } i = 1, 2, \dots, n, \quad (8)$$

where  $\rho_{\hat{\mathbf{x}}_i}$  is the distribution generated by uniform sampling on straight lines between pairs of points sampled from  $\tilde{\rho}_{t_i}$  and  $\hat{\rho}_{\mathcal{D}_i}$ , and  $\lambda = 0.1$  is the gradient penalty coefficient. Hence,

$$d(\tilde{\rho}_{t_i}, \hat{\rho}_{\mathcal{D}_i}) = -\mathbb{E}_{\tilde{\mathbf{X}}_{t_i} \sim \tilde{\rho}_{t_i}} [D_i(\tilde{\mathbf{X}}_{t_i})] + \mathbb{E}_{\mathbf{X}_{t_i} \sim \hat{\rho}_{\mathcal{D}_i}} [D_i(\mathbf{X}_{t_i})]. \quad (9)$$

Here,  $d(\tilde{\rho}_{t_i}, \hat{\rho}_{\mathcal{D}_i})$  can be mathematically interpreted as the Wasserstein distance between the two input distributions. Note that the second term in Equation 9 is independent of  $\theta$  and  $\phi$  in the generative model, and thus it can be dropped in the implementation.

Compared with WGAN-GP, the SW distance is more robust and requires less computational cost [3]. Therefore, we mainly use the SW distance to demonstrate the effectiveness of our method in numerical experiments. However, as we will find in our experiments, SW is not as scalable to high dimensional problems as WGAN-GP.

Apart from the SW distance and WGAN-GP, one can also explore using other versions of GANs or other metrics of difference, like maximum mean discrepancy (MMD), to act as the function  $\mathbf{b}$  in Equation 7. We also remark that while in this paper we use individual discriminators for each  $i$ , it is also worth comparing this strategy with conditional GANs, where only one discriminator is involved, with time  $t$  acting as the condition.

### 3.3 Augmentations to the generative model

We can also modify the generated distribution  $\tilde{\rho}_t$  as an augmentation to the generative model, in adaption to different cases, e.g., where the distributions have heavy tails, or the observations are noisy or truncated. Note that both the (squared) SW distance and the WGAN-GP can still be used as a metric for the differences.

#### 3.3.1 Push forward map for heavy tails

In some cases, especially when the stochastic term in SODE is a Lévy process,  $\rho_t$  may have heavy tails, which could spoil the training, as we will show in the computational results. To address the heavy tails, we can choose a suitable

bounded map  $h : \mathbb{R}^d \rightarrow \mathbb{R}^d$  for a  $d$ -dimensional SODE. Instead of the loss function in Equation 7, we define the loss function as:

$$L = \sum_{i=1}^n d(h_{\#}\tilde{\rho}_{t_i}, h_{\#}\hat{\rho}_{\mathcal{D}_i}), \quad (10)$$

where  $h_{\#}\tilde{\rho}_{t_i}$  is the push forward of  $\tilde{\rho}_{t_i}$  through  $h$ , similarly for  $h_{\#}\rho_{t_i}$ . In implementations, we only need to replace  $\tilde{\mathbf{X}}_{t_i}$  and  $\mathbf{X}_{t_i}$  with  $h(\tilde{\mathbf{X}}_{t_i})$  and  $h(\mathbf{X}_{t_i})$ , respectively, when calculating the loss function.

In this paper, we set  $h$  as  $h(\mathbf{x}) = a \tanh(\mathbf{x}/a)$ , where all the operations are in the element-wise sense. The selection of  $a$  depends on the  $\rho_t$ .

### 3.3.2 Perturbation for noisy data

If the observations of the particle coordinates are noisy, we can also perturb the generated samples to add “artificial” noise. More formally, instead of the loss function in Equation 7, we define the loss function as:

$$L = \sum_{i=1}^n d(\tilde{\rho}_{t_i} * \mathcal{N}_e, \hat{\rho}_{\mathcal{D}_i}), \quad (11)$$

where  $\mathcal{N}_e$  is the artificial noise with trainable variables  $e$  which should be trained together with  $\theta$  and  $\phi$ . In implementations, we only need to replace the  $\tilde{\mathbf{X}}_{t_i}$  with  $\tilde{\mathbf{X}}_{t_i} + \boldsymbol{\xi}_e^{noise}$ , where  $\boldsymbol{\xi}_e^{noise}$  are i.i.d. random samples from  $\mathcal{N}_e$ , when calculating the loss function.

For example, if the observation noise is Gaussian noise with zero mean,  $e$  would be the unknown standard deviation, and  $\boldsymbol{\xi}_e^{noise}$  can be parameterized as  $e\boldsymbol{\xi}_{\mathcal{N}}$ , where  $\boldsymbol{\xi}_{\mathcal{N}}$  are i.i.d. random samples from a  $d$ -dimensional standard Gaussian distribution.

### 3.3.3 Mask for truncated data

In some cases, we can only make observations of  $\mathbf{X}_{t_i}$  in a specific domain, denoted by  $\Omega_i$ , i.e.,  $\mathcal{D}_i$  is truncated by  $\Omega_i$ . In such cases, instead of the loss function in Equation 7, we define the loss function as:

$$L = \sum_{i=1}^n d(\tilde{\rho}_{t_i}^{\Omega_i}, \hat{\rho}_{\mathcal{D}_i}), \quad (12)$$

where  $\tilde{\rho}_{t_i}^{\Omega_i}$  is the distribution of  $\tilde{\mathbf{X}}_{t_i}$  with samples out of  $\Omega_i$  filtered out. In implementations, we only need to filter the generated  $\tilde{\mathbf{X}}_{t_i}$  with a boolean mask corresponding to  $\Omega_i$  when calculating the loss function.

We want to make a comparison between the idea of masks in this paper and the mechanism of “attention”, which is widely used in GANs for image generation tasks [26, 27]. “Attention” is usually applied so that the neural network pays more attention to a part of the input features, which is in analogy to the particle coordinates in our problem. In our method, the metric  $d$  pays attention to samples in  $\Omega_i$ , but is not biased towards any coordinate.

## 4 Computational Results

In this section, we present our computational results. All the neural networks in this section are feed-forward neural networks with three hidden layers, each of width 128. We use the leaky ReLu [28] activation function with  $\alpha = 0.2$  for the discriminator neural networks in WGAN-GP, while using the hyperbolic tangent activation function for other neural networks. The batch size is set to 1000. We use the Adam optimizer [29] with  $lr = 0.0001, \beta_1 = 0.9, \beta_2 = 0.999$  for the cases using the sliced Wasserstein distance, while  $lr = 0.0001, \beta_1 = 0.5, \beta_2 = 0.9$  for the cases with WGAN-GP.

### 4.1 1D Forward Problem

In this section, we wish to show that our method can make use of the SODE and the observations at multiple time instants to reduce the error from limited samples.

We consider the one-dimensional SODE:

$$dX_t = (4X_t - X_t^3)dt + 0.4dB_t, \quad t \geq 0, \quad (13)$$

with  $\rho_0 = 0.5\mathcal{N}(-0.5, 0.3^2) + 0.5\mathcal{N}(0.5, 0.3^2)$ .

We test the following two cases of training data sets:

Case 1: We independently draw 1000 samples from  $\rho_t$  at  $t = 0.05, 0.1, 0.15, 0.2, 0.25$ .

Case 2: We prepare 1000 sample paths, then observe all the particle coordinates at these 1000 sample paths at  $t = 0.05, 0.1, 0.15, 0.2, 0.25$ .

We assume that we know the Equation 13, but have no knowledge of  $\rho_0$ . In the context of “point-regression”, we could make the analogy of performing linear regression, where we know the slope but do not know the intercept, given some noisy observations of a linear function  $f(t)$  at different  $t$ . For each case we run our code three times with different random seeds. In Figure 3 we illustrate the density functions inferred from our method or directly from the training data at discrete time instants. In Figure 4 we show the integrated squared error of the inferred density functions.

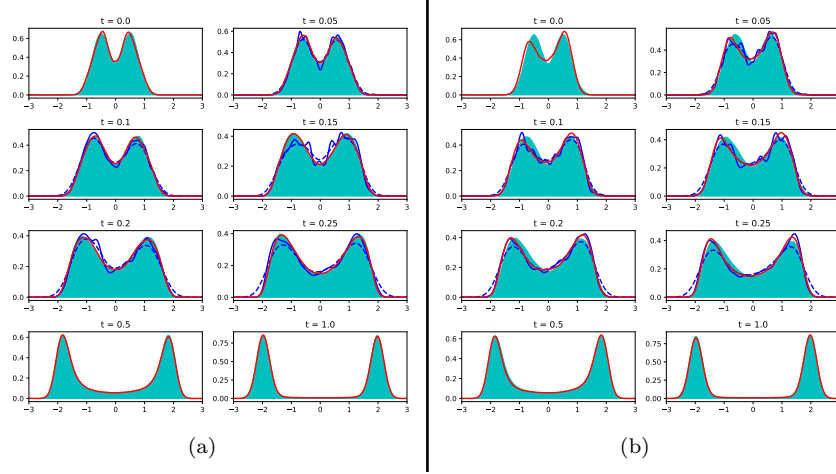


Figure 3: Density functions inferred from our method (red lines) or directly from the training data at discrete time instants (blue lines), compared with the ground truth (green areas), in (a) case 1 and (b) case 2 of the 1D forward problem. Results come from one of the three runs for each case. We use  $10^5$  samples to perform kernel density estimation with a Gaussian kernel, where the bandwidth is 0.1, according to Scotts Rule, for the inferred density and ground truth density. We use the dashed and solid blue lines to show the density estimated from 1000 training data with bandwidth  $\approx 0.25$  (according to Scotts Rule) as well as bandwidth = 0.1, respectively.

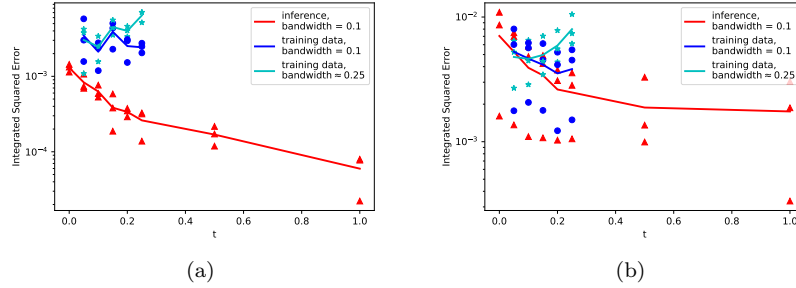


Figure 4: Integrated squared errors (ISE) of the inferred density functions at discrete times in (a) case 1 and (b) case 2 of the 1D forward problem. The squared errors are integrated from -4 to 4. The colored lines show the average ISE from three runs, while the markers with the corresponding colors show the ISE from each run. The densities are estimated in the same way as in Figure 3.

In Figure 3(a) and Figure 4(a) we can clearly see that in case 1 our method significantly outperforms the kernel density estimation using the training data,

even for  $t = 0.05$ . In experiments not shown here, we also observed significant improvement in the cases where the observations are independently drawn from a large pool of sample paths. This demonstrates the capability of our method in utilizing the SODE and the observations at multiple time instants to reduce the error from limited samples. However, in case 2 our method cannot outperform the kernel density estimation for  $t = 0.05$ , as shown in Figure 3(b) and Figure 4(b). In other words, the observations at  $t > 0.05$  do not help to infer the density at  $t = 0.05$ . This is reasonable since the observations come from the same batch of sample paths, and thus the observations at  $t > 0.05$  cannot provide additional information considering that the SODE is already known.

Let us make an analogy in the context of linear regression discussed above: if the observations have independent noise, multiple observations will be more helpful than a single observation. However, if the observations have the same noise, multiple observations cannot help us more than a single observation, considering that we already know the slope.

## 4.2 1D Inverse Problems: Brownian Noise and Lévy Noise

In this section, we test our method on the 1D inverse problem assuming incomplete knowledge of the SODE. In particular, we first consider the SODE with Brownian motion and then with the  $\alpha$ -stable symmetric Lévy process as the stochastic term:

$$\begin{aligned} dX_t &= (X_t - X_t^3)dt + dB_t, \\ \text{or } dX_t &= (X_t - X_t^3)dt + dL_t^\alpha, \quad t \geq 0, \end{aligned} \tag{14}$$

where  $\alpha = 1.5$ , with  $\rho_0 = \mathcal{N}(0, 0.2^2)$ .

Similar to the forward problem, we assume that we have no knowledge of  $\rho_0$ . We also assume that we know that the diffusion coefficient has constant value but we need to infer it; here the ground truth is 1.0. Specifically, we use a trainable variable rectified by a softplus function

$$\text{softplus}(x) = \ln(1 + e^x), \tag{15}$$

which ensures positivity in approximating the diffusion coefficient.

As for the drift  $\mu(x) = x - x^3$ , we consider the following two cases for both SODE problems:

Case 1: We know that the drift is a cubic polynomial of  $x$ . In this case, we use a cubic polynomial  $a_0 + a_1x + a_2x^2 + a_3x^3$  to parameterize  $\mu(x)$ , and want to infer the four coefficients  $a_0, a_1, a_2$  and  $a_3$ .

Case 2: We only know that the drift is a function of  $x$ . In this case, we use a neural network to parameterize  $\mu(x)$ .

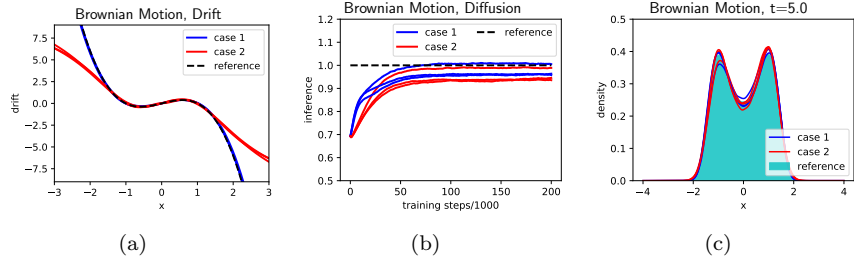


Figure 5: 1D inverse problems with Brownian motion: Inferred drift and diffusion as well as density function at  $t = 5$ . In each plot we use three lines with the same color to show the results from three runs for each case. (a) Inferred drift functions in both cases of drift parameterization. The black dashed line represents the reference ground truth. (b) Inferred diffusion coefficients during the training in both cases of drift parameterization. (c) Inferred density functions in both cases of drift parameterization, compared with the ground truth (green areas).

For the SODE problem with Brownian motion, we first prepare a pool of  $10^5$  sample paths, then independently draw 10,000 samples at  $t = 0.2, 0.5, 1.0$  from the pool as our training data. The results for both cases of drift parameterization are illustrated in Figure 5. Both cases provide a good inference of the diffusion coefficient, as shown in Figure 5(b), with an error less than 7% after  $2 \times 10^5$  training steps in all the runs. When using the cubic polynomial parameterization, the inferred drift fits well with the ground truth, with the relative  $L_2$  error about 3% in  $[-3, 3]$  averaged over three runs. The inferred drift using the neural network only fits the ground truth in the region between -1.5 and 1.5. This is reasonable since the particles mainly concentrate in this region, and we can hardly learn the drift outside this region, where the training data are sparse. Note that such an inference of drift is good enough for a good prediction of the distribution at  $t = 5$ , as shown in Figure 5(c).

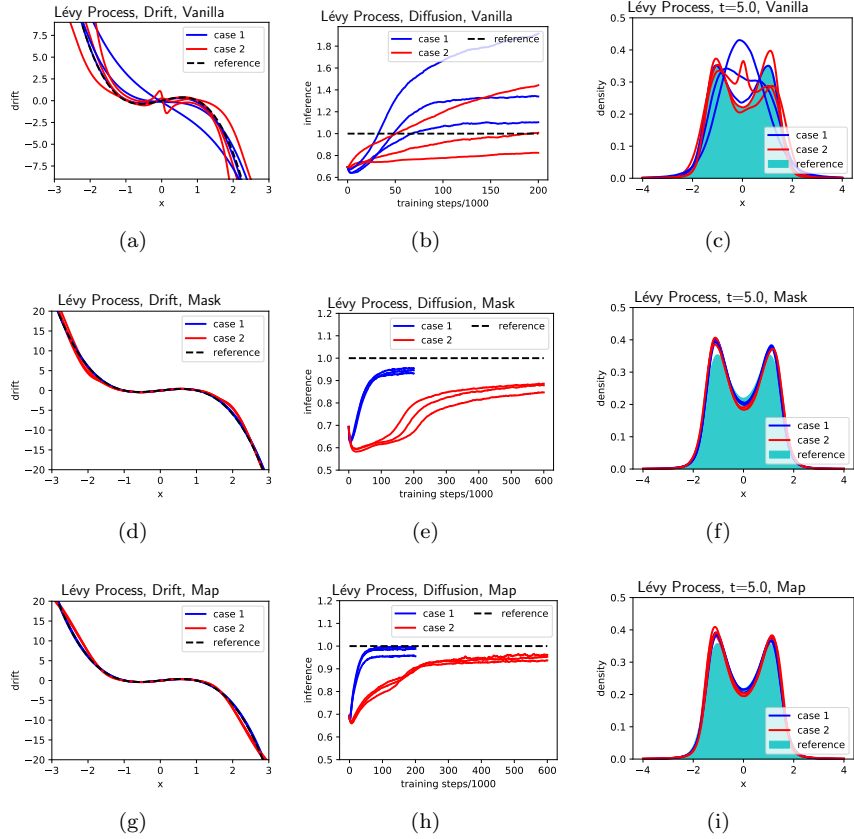


Figure 6: 1D inverse problems with Lévy process: Inferred drift and diffusion as well as density function at  $t = 5$ . Top row: vanilla method similar to the Brownian case. Middle row: with a mask. Bottom row: with a push forward map. The legend is the same as in Figure 5.

For the SODE problem with Lévy process, we prepare  $1.5 \times 10^5$  sample paths, then independently draw 10,000 samples within the region  $[-1000, 1000]$  at  $t = 0.2, 0.5, 1.0$  from the pool as our training data. We clipped the generated  $\alpha$ -stable random variable in Equation 4 between  $-100$  and  $100$  and used double precision to prevent instability during the training.

We first use the same method as for the SODE problem with Brownian motion, and refer it to the “vanilla” method. The results are shown in the first row of Figure 6. As we can see, the inferences are much worse than those in the problem with Brownian motion. We attribute this to the heavy tail of  $\rho_t$  in the Lévy process: some samples far away from 0, although rare, could dominate the loss function and spoil the training, especially in our case using sliced Wasserstein distance as the loss.

We compare two approaches to address the issue of heavy tails. We first

use a mask to truncate the heavy tails for both training data and the generated samples, as introduced in Section 3.3.3. In particular, we set  $D_i = [-3, 3]$  for  $i = 1, 2, 3$ . The results are shown in the second row of Figure 6, where we can see the inferences are much better than those from the vanilla method. As an alternative, we apply a push forward map as is introduced in Section 3.3.1, with  $h$  set as  $h(x) = 2 \tanh(x/2)$ . The results are shown in the bottom row of Figure 6. While the inferred drift function is similar to that from the method with a mask, the inferred diffusion is much better, and thus is recommended as a solution for the issue of heavy tails. One interesting observation is that in case 2 where the drift is parameterized by neural networks, although the convergence is slower, the inferred drift is better than that in the SODE problem with Brownian motion. This is because the samples are more scattered in the Lévy case.

### 4.3 2D inverse problem

In this section, we test our method on a 2D inverse problem assuming that the drift and diffusion in the two dimensions are correlated. Specifically, we consider the following 2D SODE:

$$d\mathbf{X}_t = \boldsymbol{\mu}(\mathbf{X}_t)dt + \begin{bmatrix} s_0 & 0 \\ s_1 & s_2 \end{bmatrix} d\mathbf{B}_t \quad (16)$$

where

$$\boldsymbol{\mu}(\mathbf{x}) = \nabla_{\mathbf{x}}\varphi(\mathbf{x}), \quad (17)$$

and

$$\begin{aligned} \varphi(\mathbf{x}) = & -(x_1 + a_0)^2(x_2 + a_1)^2 \\ & - (x_1 + a_2)^2(x_2 + a_3)^2 \quad \text{for } \mathbf{x} = (x_1, x_2), \end{aligned} \quad (18)$$

where  $a_0 = a_1 = 1.0, a_2 = a_3 = -0.5$ . We set the initial distribution as  $\rho_0 = \mathcal{N}(0, \mathbf{I}_2)$ . We assume that we know that the diffusion coefficient is a constant lower triangular matrix but we need to infer the three unknown parameters  $s_0, s_1, s_2$ . In particular, we use  $(\text{softplus}(\tilde{s}_0), \tilde{s}_1, \text{softplus}(\tilde{s}_2))$  to approximate  $(s_0, s_1, s_2)$ , where  $\tilde{s}_0, \tilde{s}_1, \tilde{s}_2$  are three trainable variables. The softplus functions applied to  $\tilde{s}_0$  and  $\tilde{s}_2$  are for guaranteeing the positivity of the diagonal terms.

As for the drift, we consider the following two cases:

Case 1: We know that the form of  $\boldsymbol{\mu}$  and  $\varphi$  in Equation 17 and 18 but we need to infer  $a_0, a_1, a_2$  and  $a_3$ . In particular, we use four trainable variables to approximate them.

Case 2: We only know that  $\boldsymbol{\mu}$  is a gradient of  $\varphi$  in Equation 17, but we have no knowledge of  $\varphi$ . In this case, we use a neural network, which takes  $\mathbf{x} \in \mathbb{R}^2$  as input and outputs a real number, to parameterize  $\varphi$ .

We prepare  $10^5$  sample paths, then we make observations of all the particle positions at  $t = 0, 0.1, 0.2, 0.3, 0.5, 0.7, 1.0$  as our training data. Note that we still do not know the analytical expression of  $\rho_0$ , similar to what we assumed



in the 1D inverse problem. In Figure 7 we visualize  $\rho_t$  and  $\tilde{\rho}_t$  in both cases, where we can see that  $\tilde{\rho}_t$  matches  $\rho_t$  for each  $t$  as we expected. The inferred drift and diffusion are illustrated in Figure 8. In case 1, all the inferred drift and diffusion parameters approach the ground truth during the training (shown in Figure 8(a) and 8(b)), with relative error less than 0.3% for each  $a_i$  and less than 4% for each  $\sigma_i$  after  $2 \times 10^5$  training steps. The inferred drift field also matches almost perfectly with the ground truth as shown in Figure 8(d). In case 2, the inferred diffusion parameters still approach the ground truth (shown in Figure 8(c)), with error comparable with that in case 1. In the region where the training data are dense (i.e., the density of the concatenation of all training data is no less than 0.05), the inferred drift field also fits well with the ground truth (Figure 8(e)), with relative mean-squared-error about 0.02. However, the inference is much worse in other regions shown in Figure 8(f). The reason is the same as in the 1D inverse problem, i.e., the neural network can hardly learn the drift field where the training data are sparse.

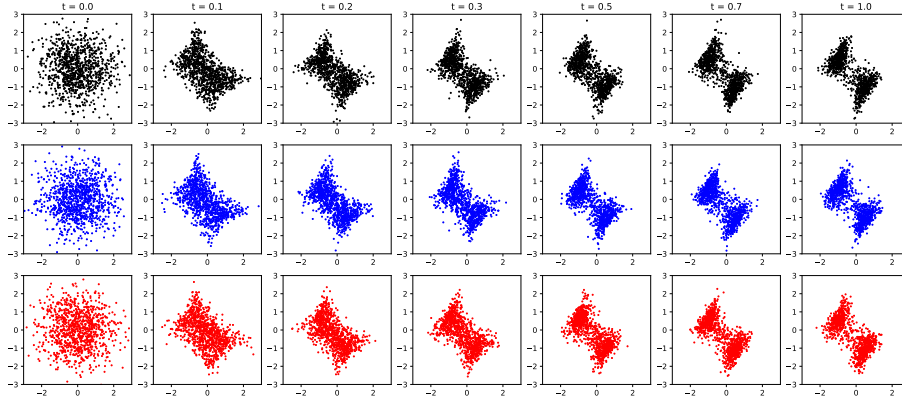


Figure 7: 2D inverse problem: Samples of (top row)  $\rho_t$ , (mid row)  $\tilde{\rho}_t$  in case 1, and (bottom row)  $\tilde{\rho}_t$  in case 2. We draw samples from  $\tilde{\rho}_t$  after  $2 \times 10^5$  training steps.

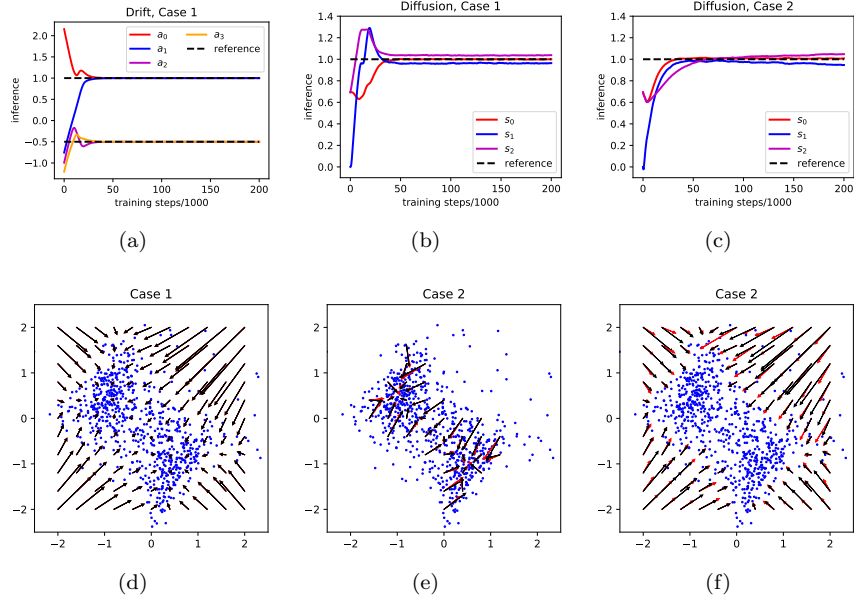


Figure 8: 2D inverse problem: Inferred drift and diffusion. (a) Inferred drift parameters in case 1, where the drift is parameterized by 4 parameters. (b) Inferred diffusion parameters in case 1. (c) Inferred diffusion parameters in case 2, where the drift is parameterized by a neural network. (d) Visualization of the inferred drift field and the exact drift field in case 1. The red and black arrows represent the inferred drift and the exact drift, respectively, the same as in (e) and (f). For each arrow, the length represents the norm of the drift at the starting point of the arrow, scaled by 0.02. The blue dots are samples from the training data, the same as in (e) and (f). (e) Visualization of the inferred drift field and the exact drift field in case 2, focusing on the region with dense training data. The lengths of the arrows are scaled by 0.1. (f) Visualization of the inferred drift field and the exact drift field in case 2, focusing on the region with sparse training data. The lengths of the arrows are scaled by 0.02.

#### 4.4 2D inverse problems with noisy or truncated data

In this section, we test our method on the 2D inverse problem where the observations are noisy or truncated. Specifically, we consider the same SODE problem as in Section 4.3, and also prepare  $10^5$  sample paths. We consider the following two scenarios of the observations at  $t = 0, 0.1, 0.2, 0.3, 0.5, 0.7, 1.0$  for our training data:

1. We make observations of all the particle coordinates, but each coordinate is perturbed by an i.i.d. random noise  $\mathcal{N}(\mathbf{0}, e\mathbf{I}_2)$ , where  $e$  is set as 0.2.
2. We make observations of the particle coordinates in  $\Omega = (\infty, 0.5) \times \mathbb{R}$ ,

with the particles outside of  $\Omega$  dropped.

We then use the techniques introduced in Section 3.3.2 and 3.3.3 to deal with the above two scenarios, respectively, aiming to learn the parameters  $a_0, a_1, a_2, a_3, s_0, s_1$  and  $s_2$  in Equation 16 and 17, as well as the standard deviation of the observation noise  $e$  in the first scenario. We show the results in Figure 9. In the first scenario, all the eight parameters converge to ground truth, with error less than 1% for each drift parameter  $a_i$ , less than 3% for each diffusion parameter  $s_i$ , and about 5% for the noise parameter  $e$ , after  $2 \times 10^5$  training steps. In the second scenario, the inferred drift parameters still match well with the ground truth, with errors less than 4% in the end, but the inferred diffusion coefficients are much worse, with an error about 13% for  $s_1$ . We also remark that we failed to learn the drift with neural network parameterization as in Section 4.3, suggesting that the method still needs further improvements.

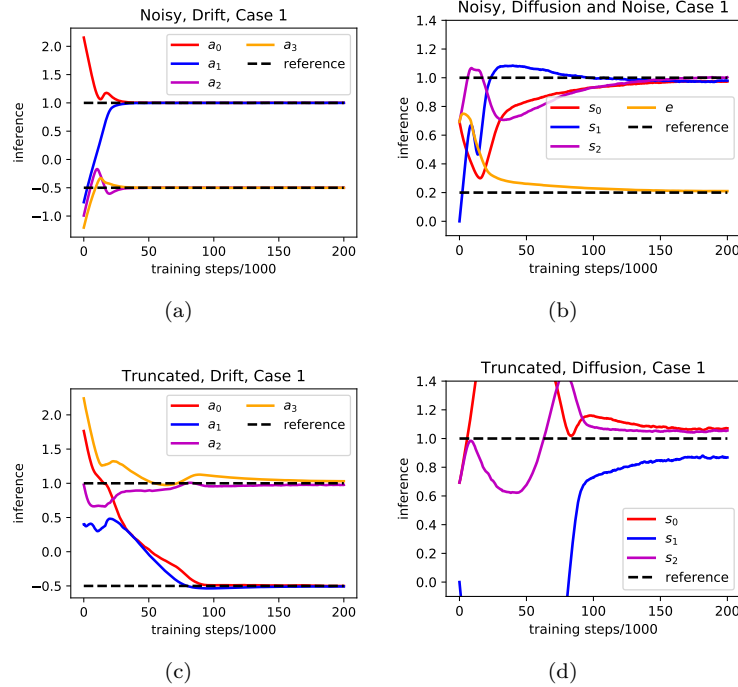


Figure 9: 2D inverse problems with noisy data (first row) or truncated data (second row): Inferred parameters in drift, diffusion and observation noise. Note that  $(a_0, a_1)$  and  $(a_2, a_3)$  are exchangeable.

## 4.5 Higher dimensional inverse problems

In this section, we test our method on higher dimensional problems. We first consider the following SODE problem, where the motions are uncoupled between

dimensions:

$$dX_t^{(i)} = (X_t^{(i)} - (X_t^{(i)})^3)dt + dB_t^{(i)}, i = 1, 2, \dots, n \quad (19)$$

where  $X_t^{(i)}$  is the  $i$ -th component of  $\mathbf{X}_t \in \mathbb{R}^d$ . We set  $\rho_0 = \mathcal{N}(\mathbf{0}, 0.04\mathbf{I}_n)$ . We prepare  $10^5$  sample paths and observe all the particle positions at  $t = 0.2, 0.5, 1.0$  as our training data.

We use a cubic polynomial of  $X_t^{(i)}$  with four trainable variables to parameterize the  $i$ -th component of the drift. Moreover, we use a trainable variable rectified by a softplus function to approximate the diffusion coefficient in each direction. As a consequence, we use  $5n$  variables to parameterize the  $d$ -dimensional SODE. Similar to the aforementioned inverse problems, we do not know  $\rho_0$ .

We firstly use the SW distance as the metric of the difference between distributions. The results are shown in Figure 10(a) and 10(b). While the SW distance works for low dimensional problems, it does not scale well to high dimensional problems. To search for an improvement, we switched to WGAN-GP to provide the metric of the difference between distributions. We show these results in Figure 10(c) and 10(d). We note that for higher dimensional problems, WGAN-GP not only converges much faster, but also gives much better inference of the drift as well as the diffusion. Even for the 20-dimensional problem, after  $2 \times 10^5$  training steps, the error of the diffusion is less than 0.06 for each dimension, with an average error of about 0.03 over the dimensions. The relative  $L_2$  error of the drift on the interval  $[-3, 3]$  is less than 8% for each dimension, with an average error of about 3% over the dimensions.

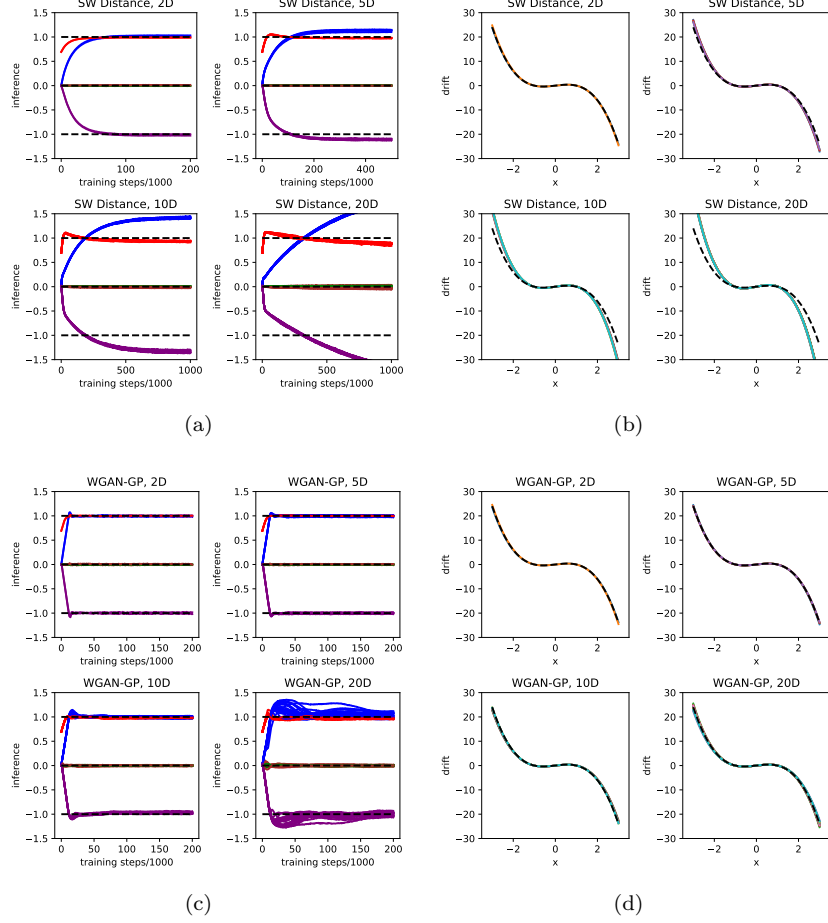


Figure 10: Results of 2D, 5D, 10D and 20D inverse problems where the motions are uncoupled between dimensions, using (a,b) the SW distance or (c,d) WGAN-GP for a metric of difference between distributions. (a) Inferred parameters during the training using SW distances. We use the green, blue, brown and purple lines to represent the inferred zero, first, second and third order coefficient in the cubic polynomial parameterization of drift, respectively. We use the red lines to represent the inferred diffusion coefficient. The multiple lines with the same color represent the coefficient in different dimensions. Similarly for (c). (b) Inferred drift function at the end of training using the SW distance. We use lines with different colors (but severely overlapped) to represent the drift function in different dimensions. Similarly for (d).

We then test our method with WGAN-GP on a more difficult problem where the motions are coupled between dimensions. In particular, we consider a  $d$ -

dimensional SODE:

$$d\mathbf{X}_t = \boldsymbol{\mu}(\mathbf{X}_t)dt + \boldsymbol{\sigma}d\mathbf{B}_t \quad (20)$$

where

$$\mu^{(i)}(\mathbf{X}_t) = X_t^{(i)} - (X_t^{(i)})^3, i = 1, 2, \dots, n, \quad (21)$$

for  $\mu^{(i)}$  as the  $i$ -th component of  $\boldsymbol{\mu}$ . In other words, the drift is the same as in 19. We also assume the diffusion coefficient matrix is

$$\boldsymbol{\sigma} = \begin{bmatrix} s_1 & 0 & 0 & 0 & \cdots & 0 \\ s'_2 & s_2 & 0 & 0 & \cdots & 0 \\ 0 & s'_3 & s_3 & 0 & \cdots & 0 \\ 0 & 0 & s'_4 & s_4 & \cdots & 0 \\ \vdots & \vdots & \vdots & \vdots & \ddots & \vdots \\ 0 & 0 & 0 & \cdots & s'_d & s_d \end{bmatrix}, \quad (22)$$

where the ground truths for the  $2d - 1$  nonzero entries  $\{s_i\}_{i=1}^d$  and  $\{s'_i\}_{i=2}^d$  are set as 1.

We prepare  $10^5$  sample paths and observe all the particle positions at  $t = 0.2, 0.5, 1.0$  as our training data, which are the same as the above uncoupled problem. We also use the same way as above to parameterize the drift, while using  $2n - 1$  trainable variables to approximate the nonzero entries in the diffusion coefficient matrix, with the diagonal entries rectified by a softplus function. As a consequence, we use  $6n - 1$  variables to parameterize the  $d$ -dimensional SODE. Here too, we assume that we do not know  $\rho_0$ .

The results are shown in Figure 11, where we can see that inference is as good as for the uncoupled case. For the 20-dimensional problem, after  $2 \times 10^5$  training steps, the error of the diffusion coefficient is less than 0.07 for each entry, with an average of 0.03 over the entries, and the relative  $L_2$  error of the drift on the interval  $[-3, 3]$  is less than 4% for each dimension, with an average error of about 2% over the dimensions. We remark that we encountered an instability for higher dimension problems.

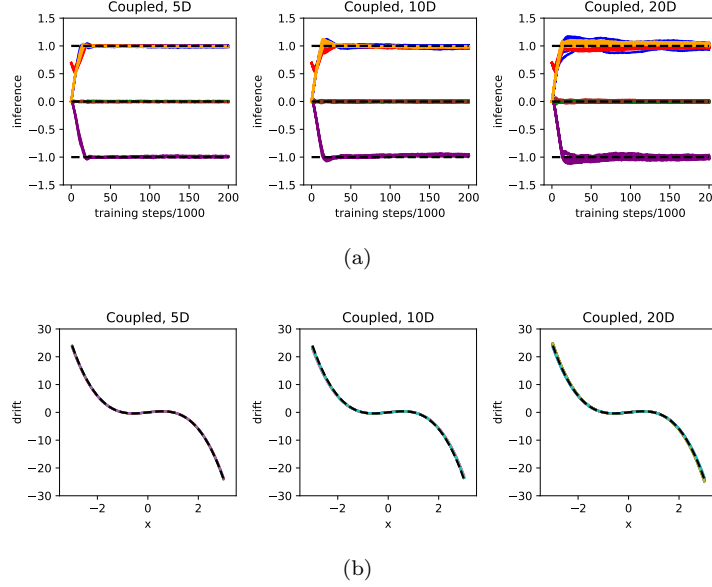


Figure 11: Results of 5D, 10D and 20D inverse problems where the motions are coupled between dimensions, using WGAN-GP for a metric of difference between distributions. (a) Inferred parameters during the training. We use the green, blue, brown and purple lines to represent the inferred zero, first, second and third order coefficient in the cubic polynomial parameterization of drift, respectively. The multiple lines with the same color represent the coefficient in different dimensions. We use the red lines to represent the inferred  $\{s_i\}_{i=1}^d$  and orange lines to represent the inferred  $\{s'_i\}_{i=2}^d$ . (b) Inferred drift function at the end of training. We use lines with different colors (but severely overlapped) to represent the drift function in different dimensions.

It may seem unrealistic that we can solve a 20-dimensional problem with only  $10^5$  samples since usually an exponentially large number of samples is required to describe the distribution. However, we remark that the effective number of degrees of freedom is substantially reduced by encoding the partial knowledge into the generator, hence the reduced number of required samples.

## 5 Paired Observations

We should note that the convergence of the marginal distribution in each snapshot does not necessarily lead to the convergence of the joint distribution of coordinate tuples  $(\mathbf{X}_{t_1}, \mathbf{X}_{t_2} \dots \mathbf{X}_{t_n})$ , which is not available in our problem setup. In the cases where the observed particle coordinates are paired across snapshots, while the method introduced in this paper still applies, it is possible to improve the inference by fitting the joint distribution of coordinate tuples from all the

snapshots with the generated ones.

In [30], the authors pointed out that due to the Markovian property of the dynamical system, this is equivalent to fitting the joint distributions of coordinate pairs  $(\mathbf{X}_{t_i}, \mathbf{X}_{t_{i+1}})$  in *adjacent* snapshots with the generated ones, which should be easier due to the reduction of the effective dimensionality<sup>2</sup>. The equivalence could be derived from the  $\alpha$ -subadditivity, which holds for KL or Jeffrey divergences as the metrics of differences. The  $\alpha$ -subadditivity was also proved in [30] for the Wasserstein distance for finite discrete sample spaces. Here, we present a theorem for the convergence in Wasserstein distance for continuous sample spaces:

**Theorem 1.** *Let  $(X_1, X_2, \dots, X_T)$  be a Markov chain of length  $T \geq 3$  and we use  $X_{i:j}$  to denote the nodes  $(X_i, X_{i+1}, \dots, X_j)$ , for  $i \leq j$ . Suppose the domain  $D_t$  for  $X_t$  is a compact subset of  $\mathbb{R}^{d_t}$  for  $t = 1, 2, \dots, T$ . We use the  $l_q$  ( $q \geq 1$ ) Euclidean metric for all the Euclidean spaces with different dimensions.*

*Let  $\{P_n^{X_{i:j}}\}_{n=1}^\infty$  and  $P^{X_{i:j}}$  be probability measures of  $X_{i:j}$  for  $i \leq j$ ,  $P_n^{X_i|X_j}$  and  $P^{X_i|X_j}$  be the corresponding probability transition kernels. If  $P_n^{X_{t:t+1}}$  converges to  $P^{X_{t:t+1}}$  in Wasserstein- $p$  ( $p \geq 1$ ) metric for all  $t = 1, 2, \dots, T-1$ ,  $P_n^{X_t|X_{t+1}}$  and  $P^{X_{t+2}|X_{t+1}}$  are  $C$ -Lipschitz continuous<sup>3</sup> in Wasserstein- $p$  metric for all  $t = 1, 2, \dots, T-2$  and  $n$ , where  $C$  is a constant, then  $P_n^{X_{1:T}}$  converges to  $P^{X_{1:T}}$  in Wasserstein- $p$  metric.*

We present the proof for Theorem 1 in Appendix D. Different from the finite discrete case, we need an additional assumption on the continuity of the probability transition kernels. Note that the theorem does not hold without the continuity assumption, and we provide a counter-example in Appendix E.

As an illustration, we study the 1D OrnsteinUhlenbeck (OU) process:

$$dX_t = -X_t dt + \sqrt{2} dW_t, \quad (23)$$

with  $\rho_0 = \mathcal{N}(0, 1)$ . Note that this setup will lead to  $\rho_t = \mathcal{N}(0, 1)$  for any  $t > 0$ . This is a special example as the governing SODE is not unique given  $\rho_t$ . We compare the inferences by matching the marginal distribution of individual coordinates or the joint distributions of adjacent coordinate pairs using the SW distance. The drift function is parameterized by a linear function  $y(x) = ax$  or a neural network, while the diffusion coefficient is represented by a trainable variable rectified by a softplus function. We present the results in Figure 12, where we can clearly see the failure in the cases of matching the marginal distribution, while matching the joint distribution works very well.

<sup>2</sup>We still can view this approach of fitting the joint distributions of coordinate pairs as “ensemble-regression”, except that instead of a curve, we try to fit the data with a *2D surface*  $(t_1, t_2) \rightarrow \rho_{t_1, t_2}$  in the probability measure space, where  $\rho_{t_1, t_2}$  denotes the joint distributions of  $(\mathbf{X}_{t_1}, \mathbf{X}_{t_2})$ .

<sup>3</sup>Note that  $P_n^{X_i|X_j}$  and  $P^{X_i|X_j}$  are functions of  $X_j$ , mapping from the Euclidean space to the probability measure space. Similar notations can be used for multiple nodes.



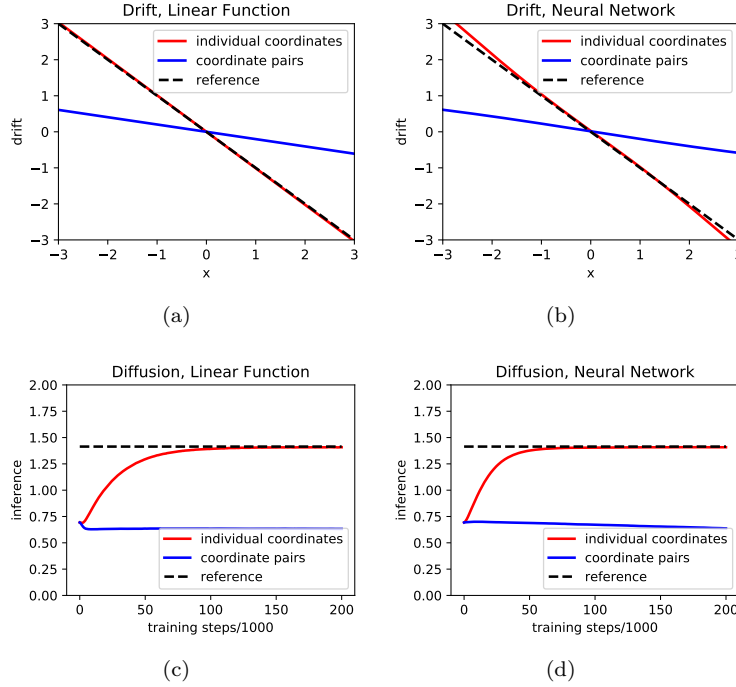


Figure 12: Inferred (first row) drift function and (second row) diffusion coefficient for the OU process, using (a,c) a linear function and (b,d) a neural network to parameterize the drift function. The red lines represent the inferences by matching the joint distributions of coordinate pairs, the blue lines represent the inferences by matching the marginal distributions, the black dashed lines represent the reference ground truths  $y(x) = -x$  for the drift function and  $\sqrt{2}$  for the diffusion coefficient.

## 6 Summary and Discussion

We have proposed a new method for inferring the governing stochastic ordinary differential equation (SODE) of particles from *unpaired observations* of their coordinates at multiple time instants, namely “snapshots”. We inferred the dynamics by training a generative model encoded with our partial knowledge of the SODE, aiming to fit the observed particle ensemble distributions with a curve in the probability measure space. Different metrics, e.g. the sliced Wasserstein distance and the adversarial loss for the generator in generative adversarial networks (GANs), were employed to quantify the differences between distributions in this paper. We refer to this approach as generative “ensemble-regression”, in analogy to the classic “point-regression”, where we infer the dynamics by performing regression in the Euclidean space.

We first applied the method to a forward one-dimensional problem, where we

know the SODE but do not know the initial distribution. We demonstrated that the probability densities inferred by our method outperform the ones directly from the training data, in the cases where the samples are independent among snapshots. We then considered inverse one-dimensional and multi-dimensional problems for Brownian and Lévy noises, where we inferred the drift and the diffusion terms from a small number of snapshots, using neural networks or polynomials (depending on our prior knowledge) to parameterize the drift term. In the Lévy noise case we demonstrated that the heavy tails in the distributions could spoil the training, but we addressed this issue by truncating the heavy tails using a mask or by applying a push forward map to both the generated distribution and the target distribution, with the latter being a better choice. We also solved the inverse problems in the cases with noisy or truncated training data, by perturbing or masking the generated samples. We finally addressed high-dimensional inverse problems up to 20 dimensions, where the sliced Wasserstein distance failed but the adversarial loss in Wasserstein GANs with gradient penalty (WGAN-GP) worked well as a metric of differences between distributions.

While in this paper we tackled the inference problem from the perspective of SODEs for the particles, it is also worth tackling the same problem from the perspective of Fokker-Planck equations for the distributions, where we can apply physics-informed neural networks [31] to enforce the physical constraints. In analogy to point-regression, techniques like various regularization methods could also be applied to the ensemble-regression to avoid overfitting or improve implementability. It is also worth studying the uncertainty quantification for ensemble-regression as in point-regression [32]. Moreover, the methods introduced in our paper require further development to address instabilities for higher dimensional problems, improve the training with neural networks in the cases with noisy or truncated data, and learn more complex dynamical systems like the ones with interactive particles. We leave these possible improvements to future research.

## 7 Acknowledgement

We would like to thank Prof. Hui Wang and Ms. Tingwei Meng for carefully checking the proof of our theorem. We also want to thank Dr. Zhongqiang Zhang for helpful discussions. This work was supported by the PhILMS grant DE-SC0019453, by the OSD/ARO/MURI W911NF-15-1-0562, and by the NIH grant U01 HL142518.

## A Generate $\alpha$ -stable random variables

Since the  $\alpha$ -stable random variable generator is not directly included in TensorFlow, which is the deep learning package we used for implementing our method, we need to generate  $\alpha$ -stable random variables from other simpler random vari-

ables. In this paper, we use the following method, which is well known in the mathematical literature [33], to generate symmetric  $\alpha$ -stable random variable  $X \sim S_\alpha(1, 0, 0)$  for  $\alpha \in (0, 2]$ :

1. Generate a random variable  $V$  uniformly distributed on  $(-\frac{\pi}{2}, \frac{\pi}{2})$ .
2. Generate another independent random variable  $U$  uniformly distributed on  $(0, 1)$ , so that  $W = -\ln(U)$  is an exponential random variable independent of  $V$  with mean 1.
3. Calculate

$$X = \frac{\sin(\alpha V)}{(\cos(V))^{1/\alpha}} \times \left( \frac{\cos(V - \alpha V)}{W} \right)^{(1-\alpha)/\alpha}. \quad (24)$$

We refer the readers to [33] for more details of generating skewed  $\alpha$ -stable random variables.

## B Sliced Wasserstein Distance

In this section we introduce the sliced Wasserstein distance; specifically, we are using the sliced Wasserstein-2 distance in this paper.

Given two measures  $\mu, \nu$  on  $\mathbb{R}^d$  with finite variance, the sliced Wasserstein-2 distance between  $\mu$  and  $\nu$  is defined as

$$SW_2(\mu, \nu) = \left( \int_{\mathbb{S}^{d-1}} W_2^2(\pi_{\mathbf{e}\#}\mu, \pi_{\mathbf{e}\#}\nu) d\mathcal{H}^{d-1}(\mathbf{e}) \right)^{1/2}, \quad (25)$$

where  $W_2$  is the Wasserstein-2 distance,  $\pi_{\mathbf{e}\#}\mu$  is the push forward of  $\mu$  through the projection map  $\pi_{\mathbf{e}}$ , defined by

$$(\pi_{\mathbf{e}\#}\mu)(A) = \mu(\{\mathbf{x} \in \mathbb{R}^d : \mathbf{e} \cdot \mathbf{x} \in A\}), \forall A \in \mathcal{B}(\mathbb{R}). \quad (26)$$

$\mathcal{H}^{d-1}$  is the uniform Hausdorff measure on the sphere  $\mathbb{S}^{d-1}$ .

To estimate  $SW_2(\mu, \nu)$  from samples of  $\mu$  and  $\nu$ , we use the following method introduced in [3], where a more formal description of the algorithm is presented.

1. Draw  $b$  samples independently from  $\mu$  and  $\nu$ , denoted as  $\mathcal{U}$  and  $\mathcal{V}$ . In this paper we set the batch size  $b = 1000$ .
2. Uniformly sample  $m$  projection directions  $\{\mathbf{e}_j\}_{j=1}^m$  in  $\mathbb{R}^d$ . In this paper we set  $m = 1000$ .
3. For each random direction  $\mathbf{e}_j$ , project and sort the samples in  $\mathcal{U}$  and  $\mathcal{V}$  in the direction of  $\mathbf{e}_j$ , getting  $\{u_{i,j}\}_{i=1}^b$  and  $\{v_{i,j}\}_{i=1}^b$ , where  $u_{i,j} \leq u_{i+1,j}$  and  $v_{i,j} \leq v_{i+1,j}$  for  $i = 1, 2, \dots, b-1$ . Calculate  $L_j = \sum_{i=1}^b (u_{i,j} - v_{i,j})^2 / b$ .
4. Calculate  $L = \sum_{j=1}^m L_j / m$  as the estimation of squared  $SW_2(\mu, \nu)$ .

Compared with GANs, the sliced Wasserstein distance does not need discriminators, and thus is more robust [3]. We also report that the sliced Wasserstein distance outperforms WGAN-GP in the following 1D simple problem. We consider the SODE:

$$dX_t = adt + bdB_t, \quad t \geq 0, \quad (27)$$

with  $\rho_0 = \mathcal{N}(-0.5, 0.5)$ . We set  $a = b = 1$  so that the exact solution is

$$\rho_t = \mathcal{N}(t - 0.5, t + 0.5). \quad (28)$$

We have 10,000 samples at  $t = 0.5$  and 1.5, respectively, as the training data, and wish to infer the constant drift and diffusion coefficients. We use the Adam optimizer [29] with  $lr = 0.001, \beta_1 = 0.9, \beta_2 = 0.999$  for the case using sliced Wasserstein distance, while  $lr = 0.001, \beta_1 = 0.5, \beta_2 = 0.9$  for the case with WGAN-GP. The results are shown in Figure 13.

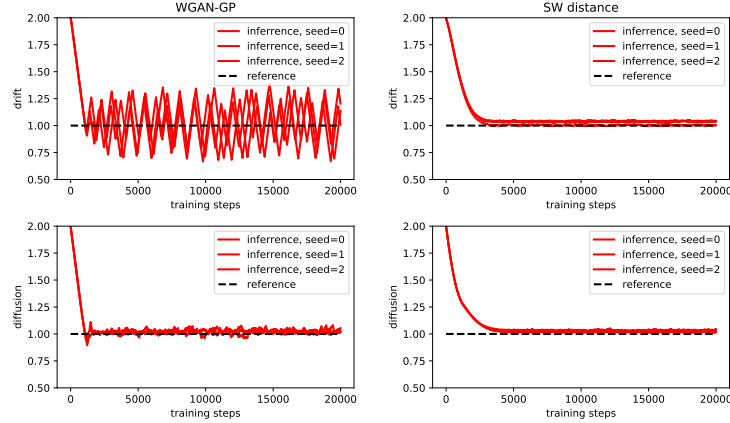


Figure 13: Inferred drift and diffusion coefficient during the training, using WGAN-GP (left) and SW distance (right).

We can clearly see oscillations of the inferred drift coefficient during the training when using WGAN-GP, but we did not see such oscillations when using the sliced Wasserstein distance. We attribute this to the two-player game between the generator and discriminator, which was reported and addressed in [34]. We also remark that we did not observe significant oscillations using WGAN-GP for generative ensemble-regression problems with dimensionality larger than one.

## C Increasing Training Data Size

In this section we study the effect of increasing training data size. In particular, we study the 2D SODE problem with the motions uncoupled between dimensions introduced in Section 4.5. We independently draw  $10^3$  to  $10^7$  samples

from  $\rho_t$  at  $t = 0.2, 0.5, 1.0$  as our training data. Apart from the cubic polynomial parameterization for the drift in each dimension, introduced in Section 4.5, we also use a neural network to parameterize the drift field mapping from  $\mathbb{R}^2$  to  $\mathbb{R}^2$ . The results are illustrated in Figure 14.

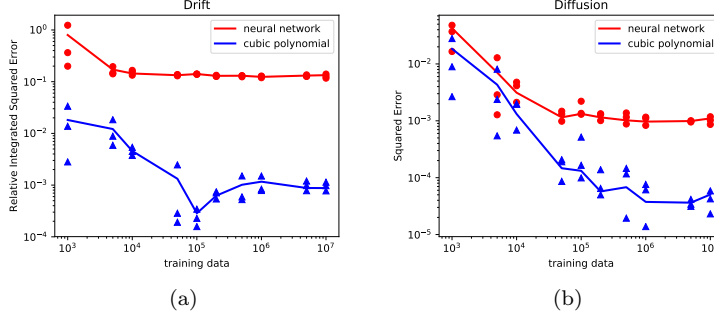


Figure 14: The results of 2D inverse problem with increasing training data size, after  $2 \times 10^5$  training steps. (a) The relative integrated squared error of drift field on  $[-2, 2]^2$ . (b) The squared error of diffusion vector coefficients. The solid line in each figure shows the error averaged over three runs with different random seeds, while the markers show the error from each run.

When parameterizing the drift with cubic polynomials, as we increase the training data, while the errors of diffusion vector coefficients show a clear decreasing trend, the errors of drift decrease first but then increase when the training data size is larger than  $10^5$ . This reminds us of the so-called “double descent” phenomenon in deep learning, but the underlying cause remains unclear. Moreover, we did not observe such a phenomenon when parameterizing the drift with a neural network.

## D Proof for Theorem 1

The proof is based on the weak convergence: convergence of a sequence of probability measures  $\{P_n\}_{n=1}^\infty$  to a probability measure  $P$  in the Wasserstein- $p$  metric is equivalent to the weak convergence plus the convergence of  $p$ -th moments of  $\{P_n\}_{n=1}^\infty$  to  $P$  [35]. Here, the weak convergence means  $E_{P_n}[f(x)]$  converges to  $E_P[f(x)]$  for each  $f \in \mathcal{F}$ , where  $\mathcal{F} = \{\text{all bounded and continuous functions}\}$  or  $\mathcal{F} = \{\text{all bounded and Lipschitz functions}\}$ , which are equivalent [36]. Note that in Theorem 1 we assume that the domain for  $X_t$  is a compact subset of Euclidean space for each  $t$ , thus  $\|X_{1:T}\|^p$  is a bounded and continuous function of  $X_{1:T}$ . The convergence of  $p$ -th moment then directly comes from the weak convergence, i.e., we only need to show that  $\{P_n\}_{n=1}^\infty$  converges to  $P$  weakly. This is proved in Lemma 4 below.

The notations are inherited from Theorem 1. For simplicity, we will sometimes use  $X, Y, Z$  to represent the nodes in sequence, and use  $P^{XY}$  to represent the probability measure of  $(X, Y)$ , etc.

**Lemma 1.** *Let  $P_y$  mapping from the Euclidean space to the probability measure space be  $C$ -Lipschitz in Wasserstein- $p$  metric ( $p \geq 1$ ). For any  $f(x, y, z) : \mathbb{R}^{d_x} \times \mathbb{R}^{d_y} \times \mathbb{R}^{d_z} \rightarrow \mathbb{R}$   $K$ -Lipschitz,*

$$g(x, y) = \int f(x, y, z) dP_y(z)$$

*is  $(C + 1)K$ -Lipschitz.*

*Proof.* Note that

$$\begin{aligned} & |g(x + \epsilon, y + \xi) - g(x, y)| \\ &= \left| \int f(x + \epsilon, y + \xi, z) dP_{y+\xi}(z) - \int f(x, y, z) dP_y(z) \right| \\ &\leq \left| \int f(x + \epsilon, y + \xi, z) dP_{y+\xi}(z) - \int f(x + \epsilon, y + \xi, z) dP_y(z) \right| + \\ &\quad \left| \int f(x + \epsilon, y + \xi, z) dP_y(z) - \int f(x, y, z) dP_y(z) \right|. \end{aligned} \tag{29}$$

Firstly

$$\begin{aligned} & \left| \int f(x + \epsilon, y + \xi, z) dP_{y+\xi}(z) - \int f(x + \epsilon, y + \xi, z) dP_y(z) \right| \\ &\leq KW_1(P_y, P_{y+\xi}) \\ &\leq KW_p(P_y, P_{y+\xi}) \\ &\leq CK\|\epsilon\|, \end{aligned} \tag{30}$$

where the first inequality comes from the KantorovichRubinstein formula [35] and that  $f(x + \epsilon, y + \xi, z)$  is  $K$ -Lipschitz. The last inequality comes from that  $P_y$  is  $C$ -Lipschitz in Wasserstein- $p$  sense.

Secondly,

$$\begin{aligned} & \left| \int f(x + \epsilon, y + \xi, z) dP_y(z) - \int f(x, y, z) dP_y(z) \right| \\ &\leq \int |f(x + \epsilon, y + \xi, z) - f(x, y, z)| dP_y(z) \\ &\leq \int K\|(\epsilon, \xi)\| dP_y(z) \\ &= K\|(\epsilon, \xi)\|. \end{aligned} \tag{31}$$

We conclude that

$$|g(x + \epsilon, y + \xi) - g(x, y)| \leq (C + 1)K\|(\epsilon, \xi)\|, \tag{32}$$

i.e.  $g(x, y)$  is  $(C + 1)K$ -Lipschitz  $\square$

**Lemma 2.** *If  $P_n^{XY}$  converge to  $P^{XY}$  weakly, then  $P_n^X$  converge to  $P^X$  weakly.*

*Proof.* For any bounded and continuous function  $f(x)$

$$\begin{aligned} & \int f(x)P_n^X(x) - \int f(x)P^X(x) \\ &= \iint f(x)P_n^{XY}(x, y) - \iint f(x)P^{XY}(x, y) \rightarrow 0. \end{aligned} \quad (33)$$

The convergence comes from the weak convergence of  $P_n^{XY}$  and that  $f(x)$  is bounded and continuous as a function of  $x$  and  $y$ .  $\square$

**Lemma 3.** *Suppose  $P_n^{YZ}$  converge to  $P^{YZ}$  weakly,  $P^{Z|Y=y}$  is Lipschitz in Wasserstein- $p$  metric. For any  $g(y, z) : \mathbb{R}^{d_y} \times \mathbb{R}^{d_z} \rightarrow \mathbb{R}$  bounded and Lipschitz, we have*

$$\begin{aligned} & \iint g(y, z)dP_n^{Z|Y=y}(z)dP_n^Y(y) \\ & - \iint g(y, z)dP^{Z|Y=y}(z)dP^Y(y) \rightarrow 0. \end{aligned} \quad (34)$$

*Proof.* Since  $g(y, z)$  is bounded and continuous, and  $P_n^{YZ}$  converge to  $P^{YZ}$  weakly,

$$\iint g(y, z)dP_n^{YZ}(y, z) - \iint g(y, z)dP^{YZ}(y, z) \rightarrow 0, \quad (35)$$

i.e.

$$\begin{aligned} & \iint g(y, z)dP_n^{Z|Y=y}(z)dP_n^Y(y) \\ & - \iint g(y, z)dP^{Z|Y=y}(z)dP^Y(y) \rightarrow 0. \end{aligned} \quad (36)$$

Since  $g(y, z)$  is bounded and Lipschitz,  $P^{Z|Y=y}$  is Lipschitz, we have

$$\int g(y, z)dP^{Z|Y=y}(z) \quad (37)$$

is Lipschitz. Further since  $P_n^Y$  converge to  $P^Y$  weakly (from Lemma 2):

$$\begin{aligned} & \iint g(y, z)dP_n^{Z|Y=y}(z)dP_n^Y(y) \\ & - \iint g(y, z)dP^{Z|Y=y}(z)dP^Y(y) \rightarrow 0. \end{aligned} \quad (38)$$

Combining 36 and 38, we have

$$\begin{aligned} & \iint g(y, z)dP_n^{Z|Y=y}(z)dP_n^Y(y) \\ & - \iint g(y, z)dP^{Z|Y=y}(z)dP^Y(y) \rightarrow 0. \end{aligned} \quad (39)$$

$\square$

**Lemma 4.** Let  $(X_1, X_2, \dots, X_T)$  be a Markov chain of length  $T \geq 3$  and we use  $X_{i:j}$  to denote the nodes  $(X_i, X_{i+1}, \dots, X_j)$ , for  $i \leq j$ . Suppose the domain  $D_t$  for  $X_t$  is a compact subset of  $\mathbb{R}^{d_t}$  for  $t = 1, 2, \dots, T$ . We use the  $l_q$  ( $q \geq 1$ ) Euclidean metric for all the Euclidean spaces with different dimensions.

Let  $\{P_n^{X_{i:j}}\}_{n=1}^\infty$  and  $P^{X_{i:j}}$  be probability measures of  $X_{i:j}$  for  $i \leq j$ ,  $P_n^{X_i|X_j}$  and  $P^{X_i|X_j}$  be the corresponding probability transition kernels. If  $P_n^{X_{t:t+1}}$  converges to  $P^{X_{t:t+1}}$  weakly for all  $t = 1, 2, \dots, T-1$ ,  $P_n^{X_t|X_{t+1}}$  and  $P^{X_{t+2}|X_{t+1}}$  are  $C$ -Lipschitz continuous in Wasserstein- $p$  metric for all  $t = 1, 2, \dots, T-2$  and  $n$ , where  $C$  is a constant, then  $P_n^{X_{1:T}}$  converges to  $P^{X_{1:T}}$  weakly.

*Proof.* We start from the case  $T = 3$ . For simplicity, we use  $X, Y, Z$  to denote the nodes in sequence.

For any  $f(x, y, z)$   $K$ -Lipschitz and bounded, we have

$$\begin{aligned} & \int f(x, y, z) dP_n^{XYZ}(x, y, z) \\ &= \int \left( \int f(x, y, z) dP_n^{Z|Y=y}(z) \right) dP_n^{XY}(x, y) \\ &= \int (g_n(x, y) - g(x, y)) dP_n^{XY}(x, y) \\ &+ \int g(x, y) dP_n^{XY}(x, y), \end{aligned} \tag{40}$$

where

$$\begin{aligned} g(x, y) &= \int f(x, y, z) dP^{Z|Y=y}(z) \\ g_n(x, y) &= \int f(x, y, z) dP_n^{Z|Y=y}(z). \end{aligned} \tag{41}$$

From Lemma 1, since  $f(x, y, z)$  is Lipschitz,  $P^{Z|Y=y}$  is Lipschitz in Wasserstein- $p$  sense, we have  $g(x, y)$  is Lipschitz.  $g(x, y)$  is also bounded since  $f(x, y, z)$  is bounded. So we have

$$\int g(x, y) dP_n^{XY}(x, y) \rightarrow \int g(x, y) dP^{XY}(x, y), \tag{42}$$

since  $P_n^{XY}$  converge to  $P^{XY}$  weakly.

We then need to show  $\int (g_n(x, y) - g(x, y)) dP_n^{XY}(x, y)$  converges to 0. We prove by contradiction. Suppose it does not converge, then there exists  $\epsilon > 0$  and a subsequence of  $n$  (denote as  $i$ ) such that

$$\left| \int (g_i(x, y) - g(x, y)) dP_i^{XY}(x, y) \right| \geq \epsilon, \forall i. \tag{43}$$

Without loss of generality, we assume that

$$\int (g_i(x, y) - g(x, y)) dP_i^{XY}(x, y) \geq \epsilon > 0, \forall i, \tag{44}$$



i.e.

$$\begin{aligned} & \iiint f(x, y, z) dP_i^{Z|Y=y}(z) dP_i^{X|Y=y}(x) dP_i^Y(y) \\ & - \iiint f(x, y, z) dP^{Z|Y=y}(z) dP_i^{X|Y=y}(x) dP_i^Y(y) \geq \epsilon > 0, \forall i. \end{aligned} \quad (45)$$

Let

$$h_i(y, z) = \int f(x, y, z) dP_i^{X|Y=y}(x), \quad (46)$$

then

$$\begin{aligned} & \iint h_i(y, z) dP_i^{Z|Y=y}(z) dP_i^Y(y) \\ & - \iint h_i(y, z) dP^{Z|Y=y}(z) dP_i^Y(y) \geq \epsilon > 0, \forall i. \end{aligned} \quad (47)$$

Note that  $f$  is  $K$ -Lipschitz,  $P_i^{X|Y=y}$  is  $K$ -Lipschitz, we have  $h_i$  are all  $K(C+1)$ -Lipschitz, thus uniformly equicontinuous. Also  $h_i(y, z)$  are uniformly bounded by the bound of  $f$ , and the domain for  $(Y, Z)$  is compact (since the domain  $D_t$  for  $X_t$  is compact for all  $t$ ). By the Arzela-Ascoli theorem, there exists a subsequence  $j$  such that  $h_j \rightarrow h$  uniformly, where  $h$  is  $K(C+1)$ -Lipschitz and bounded. Therefore,

$$\begin{aligned} & \iint (h_j(y, z) - h(y, z)) dP_j^{Z|Y=y}(z) dP_j^Y(y) \\ & - \iint (h_j(y, z) - h(y, z)) dP^{Z|Y=y}(z) dP_j^Y(y) \rightarrow 0. \end{aligned} \quad (48)$$

From Lemma 3

$$\begin{aligned} & \iint h(y, z) dP_j^{Z|Y=y}(z) dP_j^Y(y) \\ & - \iint h(y, z) dP^{Z|Y=y}(z) dP_j^Y(y) \rightarrow 0. \end{aligned} \quad (49)$$

We then have

$$\begin{aligned} & \iint h_j(y, z) dP_j^{Z|Y=y}(z) dP_j^Y(y) \\ & - \iint h_j(y, z) dP^{Z|Y=y}(z) dP_j^Y(y) \rightarrow 0. \end{aligned} \quad (50)$$

We have a contradiction between Equation 47 and 50. We finish the proof for  $T = 3$ .

We then prove the case for general  $T$  by induction. Suppose it holds for  $T = N$ , we now prove it for  $T = N + 1$ .

From the conditions for the case  $T = N + 1$  and that the theorem holds for  $T = N$ , we have  $P_n^{X_{1:N}}$  converges to  $P^{X_{1:N}}$  weakly and  $P_n^{X_{2:N+1}}$  converges to  $P^{X_{2:N+1}}$  weakly. We now view  $X_1$  as  $X$ , view the Cartesian product of  $X_{2:N}$  as  $Y$ , and view  $X_{N+1}$  as  $Z$ , so we have  $P_n^{X^Y}$  converges to  $P^{X^Y}$  weakly and  $P_n^{Y^Z}$  converges to  $P^{Y^Z}$  weakly. Also  $P_n^{X|Y}$  and  $P^{Z|Y}$  are  $C$ -Lipschitz continuous and Wasserstein- $p$  metric for all  $n$ , since  $P_n^{X|Y} = P_n^{X_1|X_2}$  and  $P^{Z|Y} = P^{X_{N+1}|X_N}$

from the Markovian property, and that  $\|X_2\| \leq \|X_{2:N}\|$ ,  $\|X_N\| \leq \|X_{2:N}\|$ . Therefore, from the theorem for  $T = 3$  case we have that  $P_n^{XYZ}$  converges to  $P^{XYZ}$  weakly, i.e.,  $P_n^{X_{1:N+1}}$  converges to  $P^{X_{1:N+1}}$  weakly.  $\square$

## E A Counterexample in Continuous Sample Space

As a direct implementation of Corollary 7 in [30], for the Markov chain  $X_{1:T}$  in a finite discrete sample space,  $P_n^{X_{t:t+1}}$  converges to  $P^{X_{t:t+1}}$  in Wasserstein- $p$  sense for each  $t = 1, 2, \dots, T-1$  implies that  $P_n^{X_{1:T}}$  converges to  $P^{X_{1:T}}$  in Wasserstein- $p$  sense. However, if the Markov chains are defined in the continuous sample space, the implementation is, in general, not correct without further assumptions, e.g., the assumption of continuity for probability transition kernels. In this section, we provide a counterexample to show that.

We consider the Markov chain with  $T = 3$  and use  $X, Y, Z$  to denote the nodes in sequence. We define  $P_n^{XYZ}$  as follows:

$$\begin{aligned} P_n^{XYZ}(0, 0, 0) &= \frac{1}{2}, \\ P_n^{XYZ}(1, \frac{1}{n}, 1) &= \frac{1}{2}, \end{aligned} \tag{51}$$

and  $P^{XYZ}$  as following:

$$\begin{aligned} P^{XYZ}(0, 0, 0) &= \frac{1}{4}, \\ P^{XYZ}(0, 0, 1) &= \frac{1}{4}, \\ P^{XYZ}(1, 0, 0) &= \frac{1}{4}, \\ P^{XYZ}(1, 0, 1) &= \frac{1}{4}. \end{aligned} \tag{52}$$

We can easily check that  $P_n^{XY}$  converges to  $P^{XY}$  in Wasserstein- $p$  metric, since

$$\begin{aligned} P_n^{XY}(0, 0) &= \frac{1}{2}, \\ P_n^{XY}(1, \frac{1}{n}) &= \frac{1}{2}, \end{aligned} \tag{53}$$

and

$$\begin{aligned} P^{XY}(0, 0) &= \frac{1}{2}, \\ P^{XY}(1, 0) &= \frac{1}{2}, \end{aligned} \tag{54}$$

Similarly  $P_n^{YZ}$  converges to  $P^{YZ}$  in Wasserstein- $p$  metric. However,  $P_n^{XYZ}$  does not converge to  $P^{XYZ}$  in Wasserstein- $p$  metric: the support of  $P_n^{XYZ}$  and  $(0, 0, 1)$  always have a distance larger than 1.

## References

- [1] Tian Qi Chen, Yulia Rubanova, Jesse Bettencourt, and David K Duvenaud. Neural ordinary differential equations. In *Advances in Neural Information Processing Systems*, pages 6571–6583, 2018.
- [2] Steven L Brunton, Joshua L Proctor, and J Nathan Kutz. Discovering governing equations from data by sparse identification of nonlinear dynamical systems. *Proceedings of the National Academy of Sciences*, 113(15):3932–3937, 2016.
- [3] Ishan Deshpande, Ziyu Zhang, and Alexander G Schwing. Generative modeling using the sliced Wasserstein distance. In *Proceedings of the IEEE Conference on Computer Vision and Pattern Recognition*, pages 3483–3491, 2018.
- [4] Ian Goodfellow, Jean Pouget-Abadie, Mehdi Mirza, Bing Xu, David Warde-Farley, Sherjil Ozair, Aaron Courville, and Yoshua Bengio. Generative adversarial nets. In *Advances in Neural Information Processing Systems*, pages 2672–2680, 2014.
- [5] Martin Arjovsky, Soumith Chintala, and Léon Bottou. Wasserstein GAN. *arXiv preprint arXiv:1701.07875*, 2017.
- [6] Ishaan Gulrajani, Faruk Ahmed, Martin Arjovsky, Vincent Dumoulin, and Aaron C Courville. Improved training of Wasserstein GANs. In *Advances in Neural Information Processing Systems*, pages 5767–5777, 2017.
- [7] David Opitz and Richard Maclin. Popular ensemble methods: An empirical study. *Journal of Artificial Intelligence Research*, 11:169–198, 1999.
- [8] Xuechen Li, Ting-Kam Leonard Wong, Ricky TQ Chen, and David Duvenaud. Scalable gradients for stochastic differential equations. *arXiv preprint arXiv:2001.01328*, 2020.
- [9] Junteng Jia and Austin R Benson. Neural jump stochastic differential equations. In *Advances in Neural Information Processing Systems*, pages 9843–9854, 2019.
- [10] Xuanqing Liu, Tesi Xiao, Si Si, Qin Cao, Sanjiv Kumar, and Cho-Jui Hsieh. Neural SDE: Stabilizing neural ODE networks with stochastic noise. *arXiv preprint arXiv:1906.02355*, 2019.
- [11] Belinda Tzen and Maxim Raginsky. Neural stochastic differential equations: Deep latent Gaussian models in the diffusion limit. *arXiv preprint arXiv:1905.09883*, 2019.
- [12] Belinda Tzen and Maxim Raginsky. Theoretical guarantees for sampling and inference in generative models with latent diffusions. *arXiv preprint arXiv:1903.01608*, 2019.

- [13] Gabriele Abbati, Philippe Wenk, Michael A Osborne, Andreas Krause, Bernhard Schölkopf, and Stefan Bauer. AReS and MaRS-adversarial and MMD-minimizing regression for sdes. In *International Conference on Machine Learning*, pages 1–10, 2019.
- [14] Ola Elerian, Siddhartha Chib, and Neil Shephard. Likelihood inference for discretely observed nonlinear diffusions. *Econometrica*, 69(4):959–993, 2001.
- [15] Bjørn Eraker. MCMC analysis of diffusion models with application to finance. *Journal of Business & Economic Statistics*, 19(2):177–191, 2001.
- [16] Simo Särkkä, Jouni Hartikainen, Isambi Sailon Mbalawata, and Heikki Haario. Posterior inference on parameters of stochastic differential equations via non-linear Gaussian filtering and adaptive MCMC. *Statistics and Computing*, 25(2):427–437, 2015.
- [17] Cedric Archambeau, Dan Cornford, Manfred Opper, and John Shawe-Taylor. Gaussian process approximations of stochastic differential equations. *Journal of Machine Learning Research*, 1:1–16, 2007.
- [18] Michail D Vrettas, Manfred Opper, and Dan Cornford. Variational mean-field algorithm for efficient inference in large systems of stochastic differential equations. *Physical Review E*, 91(1):012148, 2015.
- [19] AS Hurn and KA Lindsay. Estimating the parameters of stochastic differential equations. *Mathematics and Computers in Simulation*, 48(4-6):373–384, 1999.
- [20] Yacine Aït-Sahalia. Maximum likelihood estimation of discretely sampled diffusions: a closed-form approximation approach. *Econometrica*, 70(1):223–262, 2002.
- [21] Liu Yang, Dongkun Zhang, and George Em Karniadakis. Physics-informed generative adversarial networks for stochastic differential equations. *SIAM Journal on Scientific Computing*, 42(1):A292–A317, 2020.
- [22] Junyu Liu, Zichao Long, Ranran Wang, Jie Sun, and Bin Dong. RODE-Net: Learning ordinary differential equations with randomness from data. *arXiv preprint arXiv:2006.02377*, 2020.
- [23] Luigi Ambrosio, Nicola Gigli, and Giuseppe Savaré. *Gradient flows: in metric spaces and in the space of probability measures*. Springer Science & Business Media, 2008.
- [24] Luigi Ambrosio and Wilfrid Gangbo. Hamiltonian ODEs in the Wasserstein space of probability measures. *Communications on Pure and Applied Mathematics: A Journal Issued by the Courant Institute of Mathematical Sciences*, 61(1):18–53, 2008.

- [25] Filippo Santambrogio. {Euclidean, metric, and Wasserstein} gradient flows: an overview. *Bulletin of Mathematical Sciences*, 7(1):87–154, 2017.
- [26] Han Zhang, Ian Goodfellow, Dimitris Metaxas, and Augustus Odena. Self-attention generative adversarial networks. In *International Conference on Machine Learning*, pages 7354–7363, 2019.
- [27] Yuusuke Kataoka, Takashi Matsubara, and Kuniaki Uehara. Image generation using generative adversarial networks and attention mechanism. In *2016 IEEE/ACIS 15th International Conference on Computer and Information Science (ICIS)*, pages 1–6. IEEE, 2016.
- [28] Andrew L Maas, Awni Y Hannun, and Andrew Y Ng. Rectifier nonlinearities improve neural network acoustic models. In *Proceedings of the International Conference on Machine Learning*, volume 30, page 3, 2013.
- [29] Diederik P Kingma and Jimmy Ba. Adam: A method for stochastic optimization. *arXiv preprint arXiv:1412.6980*, 2014.
- [30] Mucong Ding, Constantinos Daskalakis, and Soheil Feizi. Subadditivity of probability divergences on Bayes-nets with applications to time series GANs. *arXiv preprint arXiv:2003.00652*, 2020.
- [31] Maziar Raissi, Paris Perdikaris, and George Em Karniadakis. Physics-informed neural networks: A deep learning framework for solving forward and inverse problems involving nonlinear partial differential equations. *Journal of Computational Physics*, 378:686–707, 2019.
- [32] Yibo Yang, Mohamed Aziz Bhouiri, and Paris Perdikaris. Bayesian differential programming for robust systems identification under uncertainty. *arXiv preprint arXiv:2004.06843*, 2020.
- [33] Aleksander Weron and Rafal Weron. Computer simulation of Lévy  $\alpha$ -stable variables and processes. In *ChaosThe Interplay between Stochastic and Deterministic Behaviour*, pages 379–392. Springer, 1995.
- [34] Constantinos Daskalakis, Andrew Ilyas, Vasilis Syrgkanis, and Haoyang Zeng. Training GANs with optimism. *arXiv preprint arXiv:1711.00141*, 2017.
- [35] Cédric Villani. *Optimal transport: old and new*, volume 338. Springer Science & Business Media, 2008.
- [36] Achim Klenke. *Probability theory: a comprehensive course*. Springer Science & Business Media, 2013.